IEEE Transactions on Automation Science and Engineering (T-ASE) paper, presented at ICRA 2026, Vienna, Austria.
Cite as T-ASE paper.

Autonomous Dental Surgery for Root Canal Treatment: Compensating for Robot-Patient Misalignment and File Deflection

Hao-Fang Cheng, Yi-Ching Ho, and Cheng-Wei Chen, *Senior Member, IEEE*

***Abstract*—Robotic technologies are increasingly used in dentistry for their precision in delicate procedures. While most dental robots focus on implant surgery, automating root canal treatment (RCT) remains challenging due to the need to guide a thin, flexible endodontic file through a narrow, curved root canal without causing ledging or file fracture. Patient movements—particularly those that induce additional file bending during insertion—further complicate robot-assisted procedures. This study presents an autonomous approach for root canal cleaning and shaping by combining force admittance and position tracking. A novel Patient Tracking Module, which connects the patient's dental brace to the robot end-effector via string potentiometers, is developed to estimate real-time robot-patient pose. Additionally, a file flexibility model is proposed to predict and compensate for file deflection during insertion. A hybrid position/force control strategy, which integrates these estimations, autonomously guides file manipulation, minimizes misalignment, and therefore reduces the risk of file fracture. Experimental validation demonstrates the system's feasibility and potential for clinical application in precision endodontic procedures.**

***Note to Practitioners*—This paper addresses the challenge of automating root canal treatment in robot-assisted endodontics, which is complicated by unpredictable patient movements and bending of endodontic files. The proposed system follows a structured workflow: (1) the dentist first diagnoses the case, labels the working length of the canal on preoperative cone-beam computed tomography (CBCT) scans, and performs access opening to the pulp chamber; (2) a custom-designed tooth brace is then installed; (3) the endodontic file held by the robot is aligned with the root canal entrance; (4) the robot is connected to the patient via a string-based Patient Tracking Module (PTM); and (5) the robot autonomously performs canal cleaning and shaping until the working length is reached. The PTM estimates patient movement in real time and compensates for it. Combined with force sensing and file deflection compensation, the system dynamically adjusts the surgical path to maintain alignment and reduce the risk of file fracture. This improves procedural safety, precision, and efficiency. Preclinical tests on acrylic models and 3D-printed teeth show promising results, but further validation in live patient settings is needed. Future work will explore automating additional steps, such as access opening and obturation, to enhance the overall treatment workflow.**

***Index Terms*—Robotic microsurgery, dental surgery, endodontic treatment, root canal cleaning and shaping, hybrid position/force control, string-based pose measurement.**

Received 13 February 2025; revised 17 June 2025 and 13 August 2025; accepted 11 September 2025. Date of publication 19 September 2025; date of current version 26 September 2025. This article was recommended for publication by Associate Editor T. L. Lam and Editor L. Zhang upon evaluation of the reviewers' comments. This work was supported in part by the National Science and Technology Council (NSTC) in Taiwan under Grant 111-2636-E-002-028, Grant 112-2628-E-002-021-MY3, Grant 113-2314-B-075-010, and Grant 114-2628-B-075-002; and in part by the Yin Shu-Tien Foundation Tapei Veterans General Hospital-National Yang Ming Chiao Tung University Excellent Physician Scientists Cultivation Program under Grant 114-V-B-033. *(Corresponding author: Cheng-Wei Chen.)*

Hao-Fang Cheng and Cheng-Wei Chen are with the Department of Electrical Engineering, National Taiwan University, Taipei 10617, Taiwan (e-mail: cwchenee@ntu.edu.tw).

Yi-Ching Ho is with the Division of Endodontics, Department of Stomatology, Taipei Veterans General Hospital, Taipei 112, Taiwan, and also with the Department of Dentistry, National Yang Ming Chiao Tung University, Taipei 30010, Taiwan.

This article has supplementary downloadable material available at https://doi.org/10.1109/TASE.2025.3611997, provided by the authors.

Digital Object Identifier 10.1109/TASE.2025.3611997

I. Introduction

SURGICAL robotics has advanced significantly, particularly in microsurgical applications where precision and repeatability surpass human capabilities [1]. However, automation in dental procedures remains limited [2]. Most existing dental robotic systems focus on implant placement, with notable examples including the FDA-approved Yomi manipulator [3] and research from institutions such as Hangzhou Normal University [4], the University of Hong Kong [5], Shanghai Jiao Tong University [6], and UCLA [7]. In contrast, automating root canal treatment (RCT) presents unique challenges due to the need to precisely guide a thin, flexible endodontic file through a narrow, curved canal while avoiding misalignment, ledging, or file fracture [8]. Unlike implant surgery, where rigid fixtures are placed in bone, RCT requires dynamic adaptation to root canal geometries and unpredictable patient movement.

RCT is performed to save a severely damaged or infected tooth—typically due to deep cavities or trauma—by removing the infected pulp, disinfecting the canals, and sealing them to prevent reinfection [8]. Performed under local anesthesia, RCT involves three main steps: (1) access opening to reach the pulp chamber; (2) cleaning and shaping to remove tissue and shape the canal; and (3) obturation to fill and seal the canal with biocompatible materials. Cleaning and shaping is the most technically challenging phase, requiring manual or engine-driven files [9] to progressively enlarge calcified and curved canals while removing debris. Dentists rely on tactile feedback rather than direct vision to precisely align and insert files. Excessive torque or lateral force can cause complications like file fracture or canal ledging [10]. Additionally, patient movement during the procedure requires manual compensation to ensure safety and accuracy.

IEEE Transactions on Automation Science and Engineering (T-ASE) paper, presented at ICRA 2026, Vienna, Austria.

Despite growing interest in dental robotics, few studies have specifically targeted the cleaning and shaping phase of RCT [11]. Early work by Dong et al. [12], [13] proposed a miniature robot mounted on teeth, but the system faced significant implementation challenges. Li et al. [14] developed a virtual endodontic training system with haptic interaction for root canal shaping. Wu et al. [15] introduced a teleoperated system with bilateral haptic feedback for canal entry localization, but it lacked autonomous navigation capabilities for curved canals. Gulrez et al. [16] achieved autonomous root canal insertion using image servo control; however, the approach was limited to transparent acrylic root canal models and is not applicable to real teeth. Dasgupta et al. [17] proposed magnetically driven nanobots for tubule disinfection, though their hyperthermia-based mechanism was too localized to address extensive bacterial contamination.

Recently, Cheng et al. [18] applied force admittance control for autonomous root canal cleaning and robot-patient alignment. However, alignment errors of up to 3 mm occurred under simulated patient motion, mainly due to the lack of modeling for canal geometry and file flexibility. Root canals taper from a wider entrance to a narrow apex [19], [20], allowing slight file misalignment without contact force. Flexible endodontic files conform to curved canals but bend excessively when misaligned laterally, producing a pronounced spring-like effect at shallow insertion depths. This effect complicates admittance controller design for force-guided alignment, as ignoring file bending causes the control response to vary with insertion depth, reducing control stability and increasing the risk of file fracture. Therefore, fully autonomous root canal treatment requires integrating position/force control with file bending compensation to ensure precise manipulation.

To overcome the limitations of force-based alignment, we propose a Patient Tracking Module (PTM) that connects the robotic manipulator to the patient's jaw via six string potentiometers, enabling real-time robot-patient pose estimation. Traditional tracking methods have notable limitations: CMM (Coordinate Measuring Machine)-type passive manipulators, commonly integrated into dental robotics, occupy considerable space, restricting their clinical usability [3], [21]. Optical markers, although more compact, are susceptible to occlusion and require clear line-of-sight [6], [22]. Multi-camera systems can alleviate occlusion issues but demand extensive setup space, further limiting practicality in clinical environments. In contrast, the proposed PTM provides a streamlined and non-intrusive solution that enhances pose estimation accuracy while preserving a compact footprint suitable for clinical applications.

In addition, we developed a file flexibility model to estimate file deflection during insertion. The compensation for file bending is integrated with a hybrid 6-DoF position/force control strategy that guides file manipulation within curved root canals and maintains accurate alignment, even in the presence of patient movement, thereby enhancing the safety and efficacy of autonomous RCT. Compared to previous work [18], which relied solely on force feedback for autonomous guidance, this study introduces the following key contributions:

1) **String-based PTM for motion tracking**: The PTM enables real-time patient motion tracking, minimizing interference while ensuring precise robot-patient alignment.
2) **Compensation for endodontic file bending**: The file deflection is estimated and compensated for, enhancing control stability and reducing the risk of fracture—particularly during shallow insertion under patient motion.
3) **Preclinical evaluation of hybrid position/force control**: The integration of position and force control demonstrates improved alignment during autonomous surgical guidance, with preclinical tests yielding promising results on acrylic models and 3D-printed teeth.

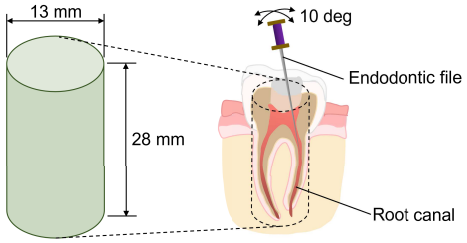

Fig. 1. RCT needs a cylindrical workspace, with a radius of 6.5 mm and a length of 28 mm, for cleaning and shaping the root canal cavity. To facilitate endodontic file insertion and manipulation during the treatment, file reorientation in roll and pitch angles should be allowed up to 10 degrees.

This article is structured as follows: Section II introduces system specifications and design; Section III presents the PTM design and kinematics; Section IV elaborates the methods for autonomous file manipulation; Section V evaluates system performance for autonomous root canal cleaning and shaping; and conclusions are provided in Section VI.

II. System Specifications and Design

This section briefly introduces the system specification, followed by the proposed system design to fulfill the clinical requirements.

A. System Specifications

For robot-assisted RCT, the system must operate within a workspace that ensures access to the entire root canal geometry while respecting anatomical constraints, particularly those imposed by the patient's mouth opening. The workspace is conservatively defined as a cylindrical volume (Fig. 1) with a 13 mm diameter—sufficient to accommodate molar-sized teeth—and a 28 mm height, reflecting the maximum reported root canal lengths [23], [24]. While this simplified cylinder does not precisely replicate the internal canal geometry, it serves as an inclusive envelope capable of covering all root canal variations.

Mouth opening limitations also constrain the robot's reachable space. The average maximum interincisal distance is 54.1 ± 6.1 mm in men and 46.9 ± 4.4 mm in women, corresponding to mandibular rotation angles of $39.1^\circ \pm 5.9^\circ$ and $36.3^\circ \pm 4.3^\circ$, respectively [25]. To accommodate these anatomical limits, the motion of the dental handpiece should be confined within a conical volume of 40 mm in diameter and a rotational span of 35°.

IEEE Transactions on Automation Science and Engineering (T-ASE) paper, presented at ICRA 2026, Vienna, Austria.

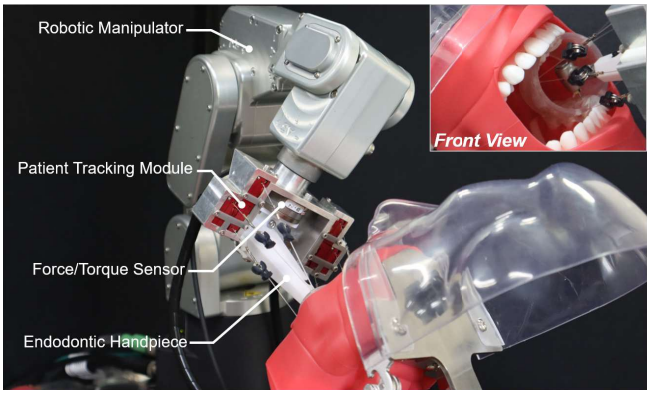

Fig. 2. Dental robot "DentiBot", designed for performing robot-assisted RCT, consists of a 6-DoF robotic manipulator, a 6-axis force/torque sensor, an endodontic handpiece, and a string-based Patient Tracking Module (PTM).

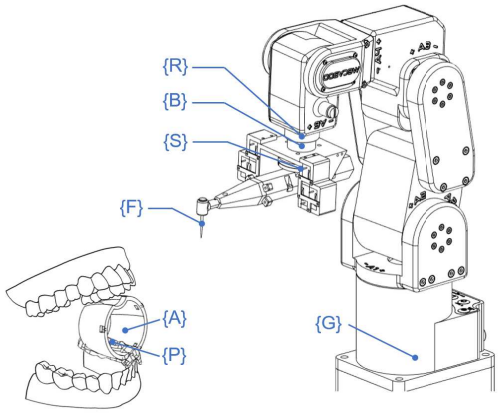

Fig. 3. Coordinate systems of the dental robot.

Precise manipulation of the endodontic file further imposes angular requirements. Due to the conical shape of root canals, a minimum roll and pitch range of 10° is necessary for effective reorientation during cleaning and shaping [26], [27]. Additionally, a full 360° yaw rotation is required to enable continuous instrumentation using NiTi rotary files (ProTaper Universal S1–F3, Dentsply Sirona, Ballaigues, Switzerland). These files are preferred for their flexibility, which helps reduce the risk of ledging [28]. They typically operate at speeds of 150–350 rpm, with safety thresholds of 3.9 N for force and 12 mN·m for torque [29], [30].

Patient motion tracking is also critical. Reported average and maximum displacement speeds are 1 mm/s and 2.5 mm/s, respectively [7]. To maintain alignment between the endodontic file and the canal entrance—approximately 1.5 mm in diameter—the system must reduce tracking error from the previously reported 3 mm [18] to 1.5 mm. When patient motion exceeds these limits, the robot should halt and allow manual intervention.

In summary, the following specifications have been defined for the dental robot:

(S1) Workspace and anatomical constraints: Defined as a 28 mm × 13 mm cylinder—accommodating all root canal geometries—with roll and pitch angles up to 10°. Motion is constrained by the mouth opening to a 40 mm diameter and 35° rotation.
(S2) Maximum lateral force and axial torque exerted to the endodontic file: 3.9 N and 12 mN·m.
(S3) Error tolerance for patient motion tracking: 1.5 mm with the maximum velocity of 2.5 mm/s.

B. Dental Robot Design

The dental robot "DentiBot" (Fig. 2) consists of a 6-DoF robotic manipulator (Meca500, Mecademic, Montreal, Canada), a custom endodontic handpiece, a 6-axis force/torque sensor (Mini40 SI-20-1, ATI Industrial Automation, Apex, NC, with the resolution of 0.01 N in force and 0.125 mN·m in torque), and a novel string-based PTM. The handpiece drives file rotation, while the manipulator controls the file orientation and its in-and-out motion for cleaning and shaping. The manipulator positions the file within a cylindrical workspace with 0.1 mm accuracy [31], meeting the workspace specification (S1).

Each component of the dental robot has its own coordinate system (Fig. 3). The robotic manipulator has its ground link serving as the fixed frame $\{G\}$. The PTM base $\{B\}$ is fixed to the sixth link $\{R\}$ of the manipulator, below which the force/torque sensor measures contact forces between the endodontic file $\{F\}$ (on the handpiece) and the root canal $\{P\}$, outputting data in the sensor frame $\{S\}$. To establish the transformation between the robot frame $\{R\}$ and endodontic file frame $\{F\}$, the tool center point (TCP) calibration [32] is applied. Note that $\{F\}$ is placed at the top of the screw-shape working part of the file, rather than the file tip.

The robotic manipulator accepts joint velocity commands $\dot{\mathbf{q}}_{\text{cmd}} \in \mathbb{R}^6$. The geometry Jacobian matrix $\mathbf{J}$ is applied to convert ${}^{\text{F}}\dot{\mathbf{p}}_{\text{cmd}} \in \mathbb{R}^6$, the velocity command along the linear (x,y,z) and rotary (ϕ,ψ,θ) axes with respect to the endodontic file frame $\{F\}$, to $\dot{\mathbf{q}}_{\text{cmd}}$, the joint velocity command:

$$\dot{\mathbf{q}}_{\text{cmd}} = \mathbf{J}^{-1} \begin{bmatrix} {}^{\text{R}}_{\text{F}}\mathbf{R} & \mathbf{0} \\ \mathbf{0} & {}^{\text{R}}_{\text{F}}\mathbf{R} \end{bmatrix} {}^{\text{F}}\dot{\mathbf{p}}_{\text{cmd}}, \tag{1}$$

$$\mathbf{J} = \begin{bmatrix} \frac{\partial {}^{\text{G}}\mathbf{p}_{\text{R}}}{\partial q_1} & \frac{\partial {}^{\text{G}}\mathbf{p}_{\text{R}}}{\partial q_2} & \cdots & \frac{\partial {}^{\text{G}}\mathbf{p}_{\text{R}}}{\partial q_6} \end{bmatrix}. \tag{2}$$

Note that $q_i \in \mathbb{R}$, $i = \{1, 2, \ldots, 6\}$, represents the angle of the i-th joint. The pose vector from the ground link to the sixth link, ${}^{\text{G}}\mathbf{p}_{\text{R}} \in \mathbb{R}^6$, is obtained from the forward kinematics of the 6-DoF robotic manipulator.

To facilitate intraoperative force guidance and meet the force/torque limit specification (S2), we use a 6-axis force/torque sensor to measure force and torque on the endodontic file. Before using these measurements, gravity compensation is performed using the method by Vougioukas et al. [33]. Next, a coordinate transformation is applied to express the compensated force/torque in the file frame $\{F\}$:

$${}^{\text{F}}\boldsymbol{f}_s = {}^{\text{F}}_{\text{R}}\mathbf{R}\, {}^{\text{R}}_{\text{S}}\mathbf{R}\, {}^{\text{S}}\boldsymbol{f}_s, \tag{3a}$$

$${}^{\text{F}}\boldsymbol{\tau}_s = {}^{\text{F}}_{\text{S}}\mathbf{R}\, {}^{\text{S}}\boldsymbol{\tau}_s + {}^{\text{F}}\mathbf{t}_{\text{S}} \times {}^{\text{F}}\boldsymbol{f}_s, \tag{3b}$$

where ${}^{\text{S}}\boldsymbol{f}_s$ and ${}^{\text{S}}\boldsymbol{\tau}_s$ represent the interaction force and torque measured in the sensor frame $\{S\}$, with gravity compensation applied. The corresponding quantities in the file frame $\{F\}$, ${}^{\text{F}}\boldsymbol{f}_s$ and ${}^{\text{F}}\boldsymbol{\tau}_s$, are used as feedback in the force control loop. Note

IEEE Transactions on Automation Science and Engineering (T-ASE) paper, presented at ICRA 2026, Vienna, Austria.

that ${}^{\mathrm{F}}_{\mathrm{R}}\mathbf{R}$ and ${}^{\mathrm{R}}_{\mathrm{S}}\mathbf{R}$ are obtained from the TCP calibration and gravity compensation processes, respectively. ${}^{\mathrm{F}}\boldsymbol{t}_s$ is determined from the CAD model. The sensor is calibrated before each use to mitigate measurement uncertainties.

On the patient side, a customized teeth anchor $\{A\}$ maintains mouth opening and surgical workspace. The PTM estimates the transformation between $\{A\}$ and $\{B\}$ in real time, while $\{R\}$ to $\{B\}$ is predefined, and $\{A\}$ to $\{P\}$ is obtained via 3D medical imaging. Consequently, the intraoperative transformation between $\{R\}$ and $\{P\}$ enables patient tracking. Section III details the PTM design and analysis.

III. String-Based Patient Tracking Module

The string-based PTM estimates and regulates the patient-robot relative pose during RCT, ensuring compliance with the patient tracking specification (S3). This section addresses key theoretical questions, including (1) mechanism design for real-time pose estimation without singularities or multiple solutions, and (2) kinematic parameter optimization to ensure clinical feasibility, sufficient estimation accuracy, and avoidance of string collisions with other strings, teeth, and the dental handpiece.

A. Mechanism Design

A string-based parallel kinematic mechanism is utilized to reduce the size of the passive pose measurement device. This mechanism estimates the relative pose between two rigid bodies by measuring the lengths of six connecting strings. Prior studies have investigated various configurations, notably the 3-2-1 and 2-2-2 types. In the 3-2-1 configuration, three ball joints are mounted on the mobile object, with three, two, and one string(s) attached to each joint, respectively [34]. The 2-2-2 configuration, alternatively, distributes the six strings equally among three ball joints [35].

However, both configurations suffer from the critical drawback of yielding multiple solutions in pose estimation. Specifically, the 3-2-1 configuration results in eight possible solutions, while the 2-2-2 configuration results in two. This ambiguity is further exacerbated when the device size is reduced, as the resulting limited string length variations cause these solutions to cluster closer together. As a result, at least two indistinguishable solutions often remain within the surgical workspace, posing a serious challenge to reliable pose estimation. Additionally, attaching multiple strings to the same ball joint not only increases installation complexity but also introduces greater susceptibility to kinematic errors.

For accurate and real-time operation, especially in dental settings, it is essential to adopt a configuration that guarantees unique and singularity-free pose estimation across the entire workspace. In this study, we employ the "1-1-1-1-1-1" configuration, where each string connects to a distinct ball joint, to develop a passive pose measurement device. The relative pose is computed using the Newton-Raphson method, which theoretically admits up to 40 solutions [36]. However, most of these are complex or can be excluded by initializing the solver near the true solution [37], effectively avoiding the issue of multiple solutions in practice.

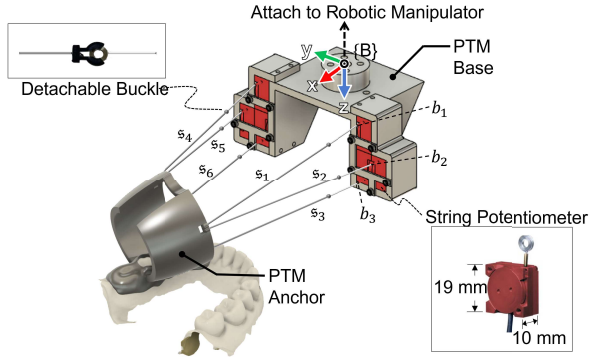

(a) Design of the PTM

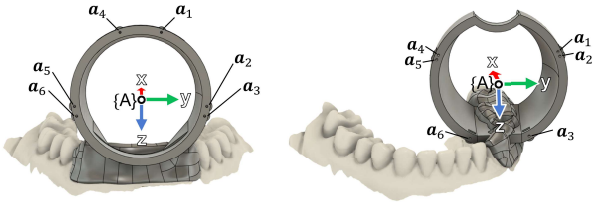

(b) String anchor design

Fig. 4. Design of the string-based Patient Tracking Module (PTM), featuring string potentiometers on the base adapter and anchors attached to the teeth. (a) Six strings ($s_i, i \in \{1, 2, \cdots, 6\}$) connect the robot to the patient, with the PTM estimating the relative pose from string lengths l_i, measured by the potentiometers. The base positions $\mathbf{b}_i$ are optimized to minimize PTM size while maximizing the spanned area to improve the sensitivity. (b) Two anchor types are designed for the anterior and posterior teeth, custom-made from 3D scans or molds for a precise fit, similar to clear aligners. A circular bite block integrated into the anchor maintains mouth openness and prevents string-lip interference. The anchor points $\mathbf{a}_i$ are placed to minimize string crossing and avoid kinematic singularities.

The proposed string-based PTM, shown in Fig. 4, incorporates six miniature string potentiometers (M150, TE Connectivity, Schaffhausen, Switzerland) with a repeatability better than 10 micrometers. Each potentiometer measures up to 38 mm and weighs 14 g. Mounted on the base adapter attached to the robotic manipulator's end effector (see Fig. 3), they are positioned to maximize the distance between each base position, i.e., the location where the string exits the potentiometer, while minimizing the adapter's size and enhancing measurement sensitivity.

The ends of the strings are securely fastened to a custom-made teeth anchor, as illustrated in Fig. 4a. This teeth anchor, crafted using a 3D printer (TOSUN Pro, FeaSun3D, Taichung, Taiwan) with FM1000 ABS-like transparent resin (shore hardness approximately 70D), is precisely customized through 3D digital scanning to match the specific contours of the patient's teeth. Similar to invisible braces (clear aligners), it conforms closely to the dentition but includes an opening for the target tooth. Integrated into the anchor is a circular bite block, which facilitates mouth opening and provides sufficient workspace for the dental handpiece. This bite block also offers a stable resting place for the upper teeth and prevents interference between the lips and the strings.

Each string is threaded through 0.5 mm diameter holes located along the circular edge of the bite block, serving as anchor points, and is secured with knots. The diameter of the holes is carefully matched to that of the strings to

IEEE Transactions on Automation Science and Engineering (T-ASE) paper, presented at ICRA 2026, Vienna, Austria.

ensure a secure fit. Two types of teeth anchors are designed (see Fig. 4b): one for the anterior teeth and another for the posterior teeth, enabling the robot to perform treatments on nearly all teeth, except last molars, which are typically the most challenging for human dentists.

To accommodate the limited stroke of the potentiometer strings, extension strings have been integrated. This ensures that the string potentiometers can operate across their full stroke range when the endodontic file, held by the dental handpiece, is inserted into the target root canal. The extension strings are made of monofilament nylon with a 0.3 mm diameter. Their lengths vary depending on the tooth position, ranging from anterior incisors to posterior molars. Nylon's low elasticity and chemical resistance ensure accurate tracking and stability during common procedures such as sodium hypochlorite irrigation. Additionally, detachable buckles have been incorporated to connect the extension strings, reducing operation time for deploying the PTM on patients. The installation of the PTM on a patient takes approximately 2 minutes for a trained dentist.

B. Kinematics Formulation

The kinematic model of the PTM is introduced in this subsection. First, the locations of the anchor points, observed in the anchor frame $\{A\}$, are defined as:

$$\mathbf{a}_i = \begin{bmatrix} 0 & r\sin\theta_i & r\cos\theta_i \end{bmatrix}^\top, \ i = 1, 2, \ldots, 6, \tag{4}$$

where r represents the radius of the circular edge on the bite block, and θ_i is the angle between the anchor point $\mathbf{a}_i$ and the negative z-axis. Note that $[\theta_1 \ \theta_2 \ \theta_3] = -[\theta_4 \ \theta_5 \ \theta_6]$ and $\theta_{min} < \theta_1 < \theta_2 < \theta_3 < \theta_{max}$, where θ_{min} and θ_{max} represent the lower and upper bounds for θ_i, respectively, to prevent overlapping with teeth. Both θ_i and r are design parameters that will be determined in Section III-C. On the other hand, the locations where the strings exit the potentiometers are defined as base positions $\mathbf{b}_i, i \in \{1, 2, \cdots, 6\}$, which are observed in the base frame $\{B\}$ and obtained from CAD model.

The PTM estimates the relative pose $\mathbf{p}_s \in \mathbb{R}^6$ between the robot and patient, representing the linear and angular displacements of the transformation matrix ${}^B_A\mathbf{T}$ between frames $\{A\}$ and $\{B\}$. This is obtained by solving the forward kinematics of the string-based parallel mechanism. To start with, the method solving for the inverse kinematics problem of the PTM is introduced: given a relative pose $\mathbf{p}_s$, the string length l_i is determined by the distance between the anchor point $\mathbf{a}_i$ and the base position $\mathbf{b}_i$:

$$l_i = \left\| ({}^B_A\mathbf{R}\,{}^A\mathbf{a}_i + {}^{\mathrm{B}}\mathbf{t}_{\mathrm{A}}) - {}^B\mathbf{b}_i \right\|_2, \ i \in \{1, 2, \ldots, 6\}, \tag{5}$$

where the translation vector ${}^{\mathrm{B}}\mathbf{t}_{\mathrm{A}}$ and rotation matrix ${}^B_A\mathbf{R}$ are derived from $\mathbf{p}_s$. The calculation of inverse kinematics is denoted as $InvKine(\mathbf{p}_s)$, which returns the six string lengths, denoted as $\mathbf{l_p} \in \mathbb{R}^6$, $\mathbf{l_p} = \begin{bmatrix} l_1 & l_2 & \cdots & l_6 \end{bmatrix}^\top$.

Given the measured string lengths $\mathbf{l} \in \mathbb{R}^6$, the forward kinematics are iteratively solved for the relative pose using the Jacobian-based Newton-Raphson method [37]. Each iteration computes the estimated string lengths $\mathbf{l_p}$ from the current pose estimate via inverse kinematics (Eq. 5), updates the pose using the string length error $\Delta\mathbf{l} = \mathbf{l} - \mathbf{l_p}$, and repeats until $\|\Delta\mathbf{l}\|_2 < tol$ (set to 1×10^{-10} mm). This procedure is summarized in Algorithm 1, where the initial guess $\mathbf{p}_{s0}$ is set to the previous estimated pose. The Jacobian matrix, which relates variations in string lengths to changes in $\mathbf{p}_s$, is computed using numerical sensitivity analysis:

$$\mathbf{J_l}(\mathbf{p}_s) = \frac{\partial \mathbf{l_p}}{\partial \mathbf{p}_s} = \frac{\partial\, InvKine(\mathbf{p}_s)}{\partial \mathbf{p}_s}. \tag{6}$$

The pose estimation is updated at a frequency of 500 Hz, with an average of 4 iterations per convergence and a total of 0.78 ms required to solve each pose on an NI LabVIEW Real-Time Target (Intel Core i7-3770 Processor).

Algorithm 1 Pose Estimation Algorithm

```
procedure PoseEst(l, p_s0, tol)
    p_s ← p_s0
    do
    l_p ← InvKine(p_s)
    Δl ← l − l_p
    p_s ← p_s + (J_l(p_s))^{-1} · Δl
    while ||Δl||_2 > tol
    return p_s
end procedure
```

C. Parameter Optimization

The placement of the PTM's anchor points directly influences the device's kinematic performance, measurement accuracy, and operational safety. The theoretical problem is to find the optimal set of anchor locations that minimizes singularities, avoids collisions, and respects sensor stroke limits across the entire surgical workspace.

Formally, the anchor points are represented as the matrix $\mathbf{A} = \begin{bmatrix} \mathbf{a}_1 & \mathbf{a}_2 & \cdots & \mathbf{a}_6 \end{bmatrix}$ and the optimization problem is defined as:

$$\mathbf{A}^* = \arg\min(loss(\mathbf{A}_k, \mathbb{P})), \tag{7}$$

where $\mathbf{A}_k$ denotes each candidate configuration and $\mathbb{P}$ is the set of $n = 1.2$ million sampled poses in the workspace, using 1 mm and 1° resolution. Each candidate is evaluated by a weighted loss function that accounts for kinematic conditioning, collision avoidance, and string displacement:

$$loss = w_1 F_1 + w_2 F_2 + w_3 F_3, \tag{8}$$

where F_1, F_2, and F_3 assess singularity, safety distance, and string displacement, respectively. The weights $w_1 = 0.4$, $w_2 = 1$, and $w_3 = 1$ reflect the relative importance of each term.

For the subfunction F_1, we aim to maximize the solvability of PTM. The solvability and dexterity of the proposed mechanism improve as the condition number of the Jacobian matrix $\mathbf{J_l}$ decreases [38]. Therefore, F_1 computes the average condition number of n different poses for the candidate $\mathbf{A}_k$:

$$F_1 = \frac{1}{n}\sum_{j=1}^{n} \mathrm{cond}(\mathbf{J_l}(\mathbf{p}_j)), \tag{9}$$

IEEE Transactions on Automation Science and Engineering (T-ASE) paper, presented at ICRA 2026, Vienna, Austria.

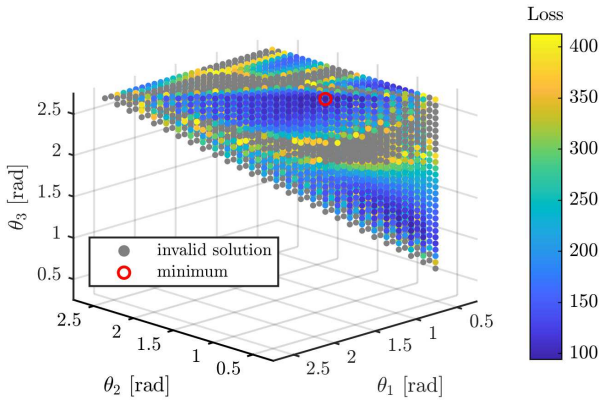

Fig. 5. The optimal radian for distributing the string anchor points on the circular bite block are chosen ($\theta_1 = 1.15$, $\theta_2 = 1.23$, and $\theta_3 = 2.67$ rad) to minimize a loss function that considers the kinematic singularity, the safety distance between the strings and the dental handpiece, and the stroke of string potentiometers. A candidate is invalid if the kinematics are singular or the string potentiometers exceed their range of motion.

where $\mathbf{J_l}(\mathbf{p}_j)$ is the Jacobian matrix at $\mathbf{p}_j$, $\mathbf{p}_j \in \mathbb{P}$. Note that the forward kinematics nearly become unsolvable if the condition number is bigger than 1000.

Second, to ensure that the strings maintain a safe and sufficient distance from each other and the handpiece, the subfunction F_2 is defined as the minimum distance between all potential collision pairs across n different poses for the candidate $\mathbf{A}_k$:

$$F_2 = -\min_{j=1}^{n} d_{min}(\mathbf{p}_j), \tag{10}$$

where $d_{min}(\mathbf{p}_j)$ represents minimum distance among all potential collision pairs at $\mathbf{p}_j$, where $\mathbf{p}_j \in \mathbb{P}$. A collision pair consists of any two segments among the six strings ($\mathfrak{s}_i, i \in \{1, 2, \cdots, 6\}$) and the six side edges of the hexagonal prism enclosing the dental handpiece ($\mathfrak{h}_i, i \in \{1, 2, \cdots, 6\}$). $\mathfrak{h}_1$, $\mathfrak{h}_2$, and $\mathfrak{h}_3$ are closer to $\mathfrak{s}_1$, $\mathfrak{s}_2$, and $\mathfrak{s}_3$, while $\mathfrak{h}_4$, $\mathfrak{h}_5$, and $\mathfrak{h}_6$ are closer to $\mathfrak{s}_4$, $\mathfrak{s}_5$, and $\mathfrak{s}_6$. As a result, there is no risk of collision between, for example, $\mathfrak{s}_1$ and $\mathfrak{h}_4$. Therefore, only 24 of the 66 possible interference pairs need to be assessed.

Finally, the subfunction F_3 is defined to penalize the maximum string displacement across n different poses:

$$F_3 = \max_{j=1}^{n} \left\| InvKine(\mathbf{p}_j) - \mathbf{l}_0 \right\|_\infty, \tag{11}$$

where $\mathbf{p}_j \in \mathbb{P}$. The string length at the initial pose, with the tip of the endodontic file positioned at the center of the cylindrical workspace, is denoted by $\mathbf{l}_0$. From this pose, each string can be extended or shortened by up to 19 mm.

To solve this nonconvex optimization problem, we perform a greedy search over 4,060 candidate anchor sets $\mathbf{A}_k$, $k \in \{1, 2, \cdots, 4060\}$, generated according to the rule specified in Eq. 4, with a 1-degree resolution for θ_i and a bite block radius r of 19 mm, selected according to the maximum mouth opening of an adult human [25]. Fig. 5 illustrates the loss values for each candidate in the design of the posterior teeth anchor, with the color of each dot indicating the respective loss. A candidate is considered invalid if it meets any of the following criteria: (1) the condition number exceeds 1000; (2) the handpiece collides with a string; or (3) the string length surpasses the maximum allowable stroke of 19 mm. The optimal anchor point locations are identified at $\theta_1 = 1.15$ rad, $\theta_2 = 1.23$ rad, and $\theta_3 = 2.67$ rad. The specific joint positions are detailed in Tab. I. The base positions $\mathbf{b}_i$ are also listed. These kinematic parameters may require a one-time calibration after fabrication and do not need to be recalibrated each time the PTM is mounted on the patient.

TABLE I

PTM String Anchor and Base Positions, in the Coordinate Frame $\{A\}$ and $\{B\}$, Respectively. Unit in Millimeters

Anchor Positions (Anterior Teeth)						
Joint	$\mathbf{a}_1$	$\mathbf{a}_2$	$\mathbf{a}_3$	$\mathbf{a}_4$	$\mathbf{a}_5$	$\mathbf{a}_6$
x	0.00	0.00	0.00	0.00	0.00	0.00
y	5.87	18.79	18.17	−5.87	−18.79	−18.17
z	−18.07	2.81	5.56	−18.07	2.81	5.56
Anchor Positions (Posterior Teeth)						
Joint	$\mathbf{a}_1$	$\mathbf{a}_2$	$\mathbf{a}_3$	$\mathbf{a}_4$	$\mathbf{a}_5$	$\mathbf{a}_6$
x	0.00	0.00	0.00	0.00	0.00	0.00
y	17.37	17.90	8.62	−17.37	−17.90	−8.62
z	−7.70	−6.37	16.93	−7.70	−6.37	16.93
Base Positions						
Joint	$\mathbf{b}_1$	$\mathbf{b}_2$	$\mathbf{b}_3$	$\mathbf{b}_4$	$\mathbf{b}_5$	$\mathbf{b}_6$
x	29.73	29.73	29.73	29.73	29.73	29.73
y	34.78	44.78	35.22	−35.22	−45.22	−34.78
z	12.41	31.41	45.59	12.41	31.41	45.59

D. Kinematic Performance Analysis

This subsection presents a comprehensive kinematic analysis of the proposed string-based PTM anchored to the posterior teeth. First, the error sensitivity of PTM estimation using the optimized configuration is examined. Second, the workspace and estimation accuracy of the proposed PTM are evaluated. Finally, we investigate the presence of any mechanical interference or string-crossing issues during the movement of the endodontic file within the designated cylindrical workspace. All simulations are conducted using the kinematic model of the dental robot, incorporating the PTM joint positions listed in Tab. I.

A Monte Carlo simulation is conducted to assess the error sensitivity of pose estimation. The estimation error is evaluated using $N = 50,000$ simulations with randomly perturbed string length measurements. Note that the actual pose was set at the origin, with an initial guess positioned 20 mm away from it. The disturbance $\epsilon_\mathbf{l} \in \mathbb{R}^6$ is generated as a uniformly distributed random numbers ranging from 0 to 0.4 mm. The simulation results, as shown in Fig. 6, reveal that only 30 out of 774 points exceed a 1 mm error when the maximum measuring error of string lengths is below 0.2 mm, which is typical for actual sensors. The maximum error in this case is 1.38 mm, meeting the accuracy requirement for patient tracking (S3).

The analysis of PTM workspace aims to ascertain its suitability for facilitating unrestricted maneuvering of the endodontic file within the prescribed cylindrical workspace. Given that the 6-DoF robotic manipulator's workspace inherently exceeds the necessary cylindrical workspace, constraints are imposed on the PTM workspace based on the 38 mm stroke limitation of the string potentiometers. This analysis is performed within a cubic box, 40 mm in width, surrounding

IEEE Transactions on Automation Science and Engineering (T-ASE) paper, presented at ICRA 2026, Vienna, Austria.

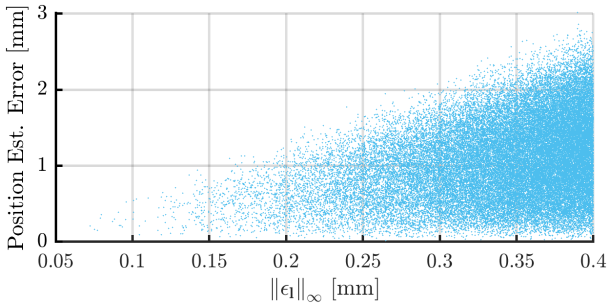

Fig. 6. Maximum position estimation errors in the Monte Carlo simulation ($N = 50,000$) with random errors in string length measurements. Note that $\|\epsilon_l\|_\infty$ denotes the maximum string length error, typically around 0.2 mm, leading to a maximum position estimation error of about 1.4 mm.

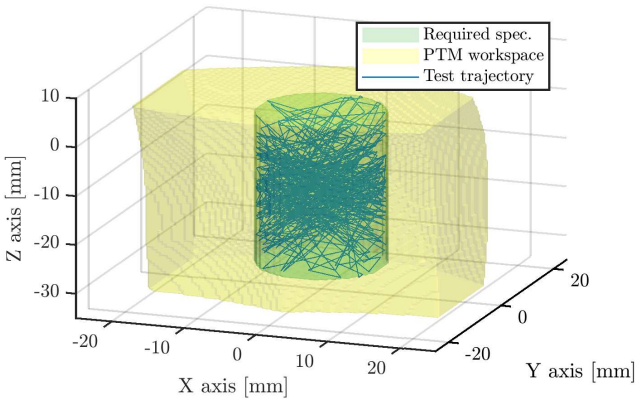

(a) PTM workspace analysis

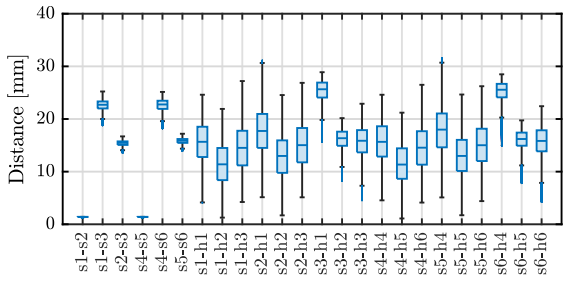

(b) String-crossing and mechanical interference analysis

Fig. 7. Kinematic performance of the PTM. (a) The required cylindrical workspace is completely confined within the volume where the PTM attains full dexterity without exceeding the maximum stroke of the string potentiometers. (b) The distances between the six strings ($\mathfrak{s}_i, i \in \{1, 2, \cdots, 6\}$) and the six side edges of the hexagonal prism enclosing the dental handpiece ($\mathfrak{h}_i, i \in \{1, 2, \cdots, 6\}$) are computed as the endodontic file follows a random test trajectory outlined in (a). The box chart of these distances shows no string crossings or collisions with the handpiece. Notably, the minimum distance of 1.1 mm (associated with pair $\mathfrak{s}_4$-$\mathfrak{h}_5$) occurs only at an extreme roll angle of the handpiece.

the cylindrical workspace, with a resolution of 0.5 mm. Dexterity, defined as the ratio of valid orientations within a $\pm$5-degree range along the roll and pitch angles, is calculated for each test point within the cube. Test points are deemed part of the PTM workspace only if they satisfy two conditions: (1) the stroke of the string potentiometers remains within the defined constraint and (2) full dexterity can be achieved at that specific point. The outcome of this workspace analysis is illustrated in Fig. 7a, where the green and yellow volumes represent the required cylindrical workspace and the PTM workspace, respectively. Importantly, the required cylindrical workspace is entirely encompassed within the region where the PTM achieves full dexterity without exceeding the maximum stroke of the string potentiometers.

Subsequently, the assessment of singularities or multiple solutions within the required cylindrical workspace for PTM estimation is conducted. In this analysis, the tip of the endodontic file undergoes random movements within the cylindrical workspace over a duration of 5000 seconds, sampled at intervals of 0.01 seconds. The maximum velocity of the dental robot is constrained to 2.5 mm/s, reflecting the maximum speed of patient movement. The test trajectory is depicted in Fig. 7a. Initially, both the starting point and the initial estimate p_{s0} are positioned at the center of the cylindrical workspace. Then, the estimated pose from the preceding timestamp serves as the initial estimate for the subsequent timestamp. Consequently, no instances of singularity or multiple solutions are observed throughout the analysis. The maximum position and orientation error along the test trajectory are 3.32×10^{-13} mm and 2.70×10^{-13} degrees, respectively.

Last, an analysis is conducted to confirm there is no string-crossing and mechanical interference when applying the PTM along with the dental robot. When analyzing the PTM estimation error along the test trajectory in the previous assessment, the distances between the six strings and the six side edges of the hexagonal handpiece are also recorded. The results, depicted in Fig. 7b, demonstrate that the distances between strings consistently exceed 1 mm. The narrowest separation between strings and the dental handpiece is 1.1 mm, observed in the case of pair $\mathfrak{s}_4$-$\mathfrak{h}_5$ during an extreme roll angle of the handpiece. This analysis confirms the absence of string interference when employing the PTM.

IV. Autonomous File Manipulation

This section presents the methods for autonomous root canal cleaning and shaping, including file flexibility compensation and a fully automated surgical workflow. Two key theoretical questions are addressed: (1) modeling file flexibility to enable real-time estimation of deflection caused by file misalignment, and (2) compensating for this deflection within a hybrid position/force control framework to achieve autonomous file alignment.

A. Endodontic File Flexibility Model

Endodontic files are flexible, enabling navigation through curved root canals, distinguishing robot-assisted RCT from automated dental implants. However, misalignment between the file and the canal, particularly when the file is only partially inserted, induces deflection in the uninserted portion and increases the risk of file fracture. This file deflection also degrades the performance of force control, making accurate estimation and compensation essential.

Fig. 8 illustrates the flexibility model of an endodontic file. As shown in Fig. 8a, the working portion of the file is approximated as a thin cone with a constant taper, where the

IEEE Transactions on Automation Science and Engineering (T-ASE) paper, presented at ICRA 2026, Vienna, Austria.

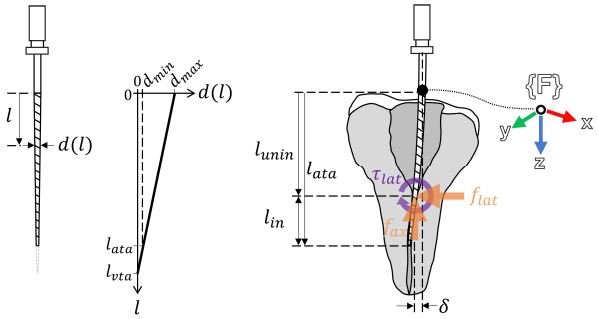

(a) Taper file (b) Deflection of file during operation

Fig. 8. Model of endodontic file flexibility. (a) A constant taper file has a decreasing diameter towards its tip. The maximum diameter d_{max} occurs at $l = 0$, while the diameter becomes zero at the virtual taper apex ($l = l_{vta}$). Note that l_{ata} denotes the actual file length. (b) The deflection δ is defined as the bending of the uninserted portion of the file due to lateral contact forces within the root canal. The contact forces/torques can be represented equivalently by a lateral force f_{lat}, an axial force f_{ax}, and an interaction torque τ_{lat}, all acting at the entrance of the root canal.

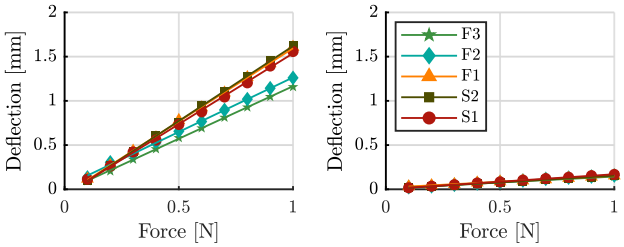

(a) Lateral Load (b) Axial Load

Fig. 9. Comparison of file deflection under lateral and axial loads shows that all file types (S1 to F3) exhibit significant deflection proportional to lateral forces, while axial forces produce negligible deflection (< 0.2 mm). Note that the lateral load is applied 3 mm from the file tip, with deflection measured by the horizontal displacement of the tip. The axial load is applied directly at the tip, and deflection is represented by the vertical displacement of the tip.

diameter d of any cross-section is modeled as a function of the length l measured from the file root,

$$d(l) = d_{max}\frac{l_{vta} - l}{l_{vta}}. \tag{12}$$

In this expression, d_{max} is the maximum diameter at the file root ($l = 0$), and l_{vta} represents the length from the file root to the virtual apex, where the cross-sectional diameter linearly decreases to zero. Note that actual files may have variable taper and non-circular cross-sections while this simplification aids analytical modeling. For example, ProTaper Universal files used in this study (Type S1–F3) have a convex triangular cross-section to minimize canal wall contact [39].

The diameter of the file tip, denoted as d_{min}, can then be expressed as

$$d_{min} = d(l_{ata}) = d_{max}\frac{l_{vta} - l_{ata}}{l_{vta}}, \tag{13}$$

where l_{ata} represents the actual length of the file.

To characterize the bending behavior of endodontic files, an experiment was conducted by applying external forces and measuring the resulting deflections. Two loading conditions were tested independently: a lateral force applied 3 mm from the file tip and an axial force applied directly at the tip. Fig. 9 presents the deflection responses of five file types (S1, S2, F1, F2, F3), ordered by increasing tip diameter. Results show a linear relationship between applied force and deflection. Lateral tip deflection is consistently greater than axial deflection across all file types; under a 1 N load, maximum axial deflection reaches only 0.17 mm—approximately ten times smaller than the corresponding lateral deflection. Theoretically, the high Young's modulus of NiTi files (20–40 GPa) limits axial compression to below 0.05 mm. However, due to slight compliance in the 3D-printed adapter, experimental values are slightly higher. Nonetheless, the file can be modeled as axially rigid, with negligible buckling effects.

During RCT, the file is inserted into the root canal along its axial direction, as illustrated in Fig. 8b. The insertion depth is denoted as l_{in}. As the file advances, it becomes obstructed when its cross-sectional diameter exceeds that of the canal entrance, at which point it begins to drill and shape the canal. Distributed contact forces arise between the file and the canal walls, with their directions tangential to the trajectory of the root canal. All contact forces and torques are equivalently represented in the frame $\{F\}$ by a lateral force f_{lat}, an axial force f_{ax}, and an interaction torque τ_{lat}, all applied at the root canal entrance.

If the file and canal are properly aligned, the net lateral force f_{lat} and interaction torque τ_{lat} should approximate zero. When the file is misaligned with the canal, the contact force with the canal walls increases, causing deflection of the uninserted portion. This study focuses on lateral deflection δ induced by f_{lat} (see Fig. 8b), assuming endodontic files tolerate greater rotational bending caused by τ_{lat}. Minimizing f_{lat} implies reduced lateral deflection and improved file alignment.

Let the lateral force and interaction torque at the root of the file, as measured by the 6-DoF force/torque sensor, be denoted as $f_{s,lat}$ and $\tau_{s,lat}$, respectively. Based on the definition in Fig. 8b, $\tau_{s,lat}$ can be expressed as

$$\tau_{s,lat} = f_{lat}l_{unin} + f_{ax}\delta + \tau_{lat}. \tag{14}$$

Assuming that δ and τ_{lat} are small, Eq. 14 is simplified and rearranged to approximate the uninserted length l_{unin} ($l_{unin} = l_{ata} - l_{in}$) as follows:

$$l_{unin} \cong \frac{\tau_{s,lat}}{f_{lat}} \cong \frac{\tau_{s,lat}}{f_{s,lat}}. \tag{15}$$

Here, $f_{lat} \cong f_{s,lat}$ since the robot operates at relatively low acceleration (typically 0.1 m/s^2).

The estimated uninserted length l_{unin} may occasionally exceed the actual file length due to the omission of the δ and τ_{lat} terms in Eq. 15, particularly when $f_{s,lat}$ is relatively small. We will later show that the adverse effect of this overestimation on control performance can be avoided. To prevent overestimation beyond the physical limit, an upper bound is imposed on l_{unin}, capping it at l_{ata}. Furthermore, the file flexibility compensator is activated only when the measured force along either the x- or y-axis exceeds a predefined threshold, which is set to 0.03 N in our system.

Next, a tapered beam deflection model [40] is revised and applied to estimate the file deflection δ:

$$\delta = f_{lat}\lambda + \frac{f_{lat}l_{unin}^3}{3E\,I(l_{unin})}\left(\frac{d(l_{unin})}{d(0)}\right)^3. \tag{16}$$

IEEE Transactions on Automation Science and Engineering (T-ASE) paper, presented at ICRA 2026, Vienna, Austria.

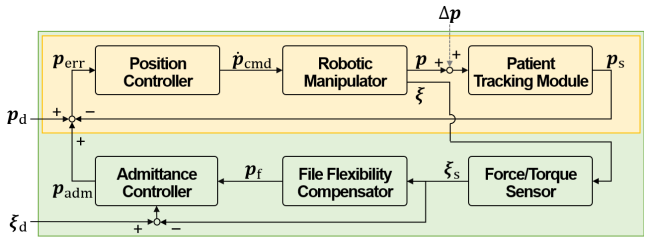

Fig. 10. Block diagram of the hybrid position/force control. In the inner-loop position control (yellow box), the manipulator regulates its relative pose $\mathbf{p}_s$ at the initial value $\mathbf{p}_d$, with $\Delta\mathbf{p}$ representing patient movement and $\mathbf{p}_s$ measured by the PTM. In the outer-loop force control (green box), the contact force $\boldsymbol{\xi}_s$ between the file and canal is measured and sent to the flexibility compensator and admittance controller, which generate pose adjustments $\mathbf{p}_f$ and $\mathbf{p}_{\text{adm}}$ to guide file manipulation and maintain alignment. Unlike pure admittance control, which maps force directly to motion, the hybrid scheme nests force-based corrections within a position loop for precise pose regulation and file alignment. A file flexibility compensator further mitigates deflection effects on control performance.

The first term represents a small deflection of the file (above the tapered part) with the spring coefficient λ. The second term describes the lateral deflection of the uninserted portion of tapered part, where E represents Young's modulus and $I(l_{unin})$ denotes the moment of inertia of the cross-sectional area,

$$I(l_{unin}) = \frac{\pi}{64}(d(l_{unin}))^4. \tag{17}$$

Eq. 16 can be rewritten after substituting Eq. 12 and Eq. 17:

$$\delta = f_{lat}\left(\lambda + \underbrace{\frac{64\ l_{vta}}{3E\pi d_{max}^4}}_{\phi}\frac{l_{unin}^3}{l_{vta}-l_{unin}}\right), \tag{18}$$

where λ, l_{vta} and ϕ are unknown constants representing file characteristics that will be determined experimentally. Given the estimated uninserted length l_{unin} (Eq. 15) and the measured lateral force $f_{s,lat}$ ($f_{lat} \cong f_{s,lat}$), this flexibility model is applied to estimate the file deflection δ along the x-axis and y-axis of the file frame $\{F\}$, respectively.

B. Hybrid Position/Force Control

To guide the file along its axial direction into the root canal while minimizing the lateral contact force $f_{s,lat}$ between the endodontic file and the canal, and simultaneously maintaining the relative robot-patient pose, a hybrid position/force control strategy is implemented. The control block diagram in Fig. 10 shows the inner and outer loops. The inner-loop position control uses pose estimation $\mathbf{p}_s$ from the PTM to track patient motion, while the outer-loop force control guides the file manipulation using force/torque measurement $\boldsymbol{\xi}_s \in \mathbb{R}^6$,

$$\boldsymbol{\xi}_s = \begin{bmatrix} \boldsymbol{f}_s \\ \boldsymbol{\tau}_s \end{bmatrix}. \tag{19}$$

This hybrid control ensures accurate pose regulation and file alignment during autonomous root canal cleaning and shaping. Critically, a file flexibility compensator is incorporated to mitigate the effects of file deflection on control performance. Note that all signals are represented in the file frame $\{F\}$.

The inner loop, running at 500 Hz, uses a proportional-derivative (PD) position controller to regulate the robot's relative pose $\mathbf{p}_s$ to the initial value $\mathbf{p}_d$. The pose error $\mathbf{p}_{\text{err}}$ is defined as the difference between $\mathbf{p}_d$ (or $\mathbf{p}_d + \mathbf{p}_{adm}$ if $\mathbf{p}_{adm}$ is a non-zero vector) and $\mathbf{p}_s$,

$$\mathbf{p}_{\text{err}}(t) = \mathbf{p}_{\text{d}}(t) + \mathbf{p}_{\text{adm}}(t) - \mathbf{p}_{\text{s}}(t). \tag{20}$$

The PD controller then computes the velocity command $\dot{\mathbf{p}}_{\text{cmd}}$ to the 6-DoF robotic manipulator as

$$\dot{\mathbf{p}}_{\text{cmd}}(t) = \mathbf{k}_p \circ \mathbf{p}_{\text{err}}(t) + \mathbf{k}_d \circ \dot{\mathbf{p}}_{\text{err}}(t), \tag{21}$$

where $\mathbf{k}_p$ and $\mathbf{k}_d$ are 6×1 gain vectors obtained via experimental tuning, and $\circ$ denotes element-wise multiplication. The use of a PD position controller is advantageous as it provides closed-loop stability, i.e., asymptotically convergence of $\mathbf{p}_{\text{err}}$, and ease of parameter tuning, while also preventing overshoot or oscillations of the file inside root canals.

For autonomous cleaning and shaping in RCT, the file manipulation is achieved by the outer force control loop. This setup is also known as "implicit force control" [41]. Specifically, the desired force/torque $\boldsymbol{\xi}_{\text{d}}$ is zero for all axes except the z-axis (file insertion) and θ-axis (file rotation). No admittance control is applied to the θ-axis to prevent interference from reactive torque during file rotation. On the other hand, the file insertion and drilling are guided by a negative desired contact force along the z-axis. In particular, if the measured force along the z-axis (i.e., f_{ax} in Fig. 8b) has not yet reached the desired setpoint, the file will engage in the root canal, allowing the canal's shape to guide the file tip toward the apex. Conversely, if the measured force exceeds the desired set value, the file will retract until the measured force returns to the desired level. Meanwhile, file misalignment induces nonzero lateral forces and torques in $\boldsymbol{\xi}_{\text{s}}$, which the admittance controller compensates for by adjusting the file's pose until proper alignment is restored and the lateral forces are minimized.

Applying admittance control and file deflection estimation, the force-guided path correction $\dot{\mathbf{p}}_{\text{adm}}$ is computed such that the measured force/torque $\boldsymbol{\xi}_{\text{s}}$ consistently converge to the desired value $\boldsymbol{\xi}_{\text{d}}$:

$$\dot{\mathbf{p}}_{\text{adm}}(t) = C_{adm}(s)\left(\boldsymbol{\xi}_{\text{d}}(t) - \boldsymbol{\xi}_{\text{s}}(t)\right) + \dot{\mathbf{p}}_f(t), \tag{22}$$

where the 6-axis admittance controller $C_{\text{adm}}(s)$ is defined as

$$C_{\text{adm}}(s) = diag\left(\frac{-k_a}{m_a s + b_a}\right), \tag{23}$$

and file deflections along the x- and y-axes (estimated using Eq. 18), denoted as δ_x and δ_y, are incorporated by

$$\dot{\mathbf{p}}_f(t) = [k_f\delta_x(t)\ k_f\delta_y(t)\ 0\ 0\ 0\ 0]^{\top}. \tag{24}$$

In Eq. 23, the mass coefficients m_a are roughly estimated from the dental handpiece's mass or rotational inertia using its 3D CAD model. The virtual damper coefficients b_a are designed to achieve a desired dynamic response, particularly in terms of settling time. The constant gain k_a, including a radians-to-degrees scaling for rotational axes, fine-tunes responsiveness to contact forces—higher k_a increases sensitivity to forces and torques. The gain k_f in Eq. 24 is used to mitigate

IEEE Transactions on Automation Science and Engineering (T-ASE) paper, presented at ICRA 2026, Vienna, Austria.

the effects of file deflection on force control, as detailed later. All parameters are tuned individually per axis to ensure smooth, safe robot-environment interaction during autonomous endodontic procedures. Eq. 23 is implemented in discrete time via bilinear transform at a 100 Hz sampling rate.

C. Force Control Analysis With File Deflection Compensation

When the endodontic file is partially inserted into root canal, its deflection significantly affects force control. As shown in Eq. 18, the deflection under a constant lateral force varies with the length of the uninserted portion:

$$\delta = f_{lat}\left(\lambda + \phi\frac{l_{unin}^3}{l_{vta} - l_{unin}}\right) := f_{lat}k_{defl}(l_{unin}), \tag{25}$$

where the spring constant k_{defl} is a function of l_{unin}. Consequently, force control response varies even under identical admittance gains. The file flexibility compensator (Eq. 24) is proposed to address this issue.

To further analyze the effect of inconsistent file bending, we examine the robot's dynamic response along the x-axis. Assuming $\mathbf{p}_s = \mathbf{p}_d$, the change rate of file misalignment, denoted as $\dot{\delta}_x(t)$, is derived by substituting Eq. 24 into Eq. 22:

$$-\dot{\delta}_x(t) = \frac{k_a}{m_a s + b_a} f_x(t) + k_f\, \delta_x(t). \tag{26}$$

Replacing $f_x(t)$ using Eq. 25 gives

$$\dot{\delta}_x(t) = -\frac{k_a}{m_a s + b_a} \cdot \frac{\delta_x(t)}{k_{defl}(l_{unin})} - k_f \delta_x(t). \tag{27}$$

Multiplying both sides by $(m_a s + b_a)$ and reorganizing terms yields the following second-order dynamical equation:

$$m_a\ddot{\delta}_x(t) + (b_a + m_a k_f)\dot{\delta}_x(t) + \left(k_f b_a + \frac{k_a}{k_{defl}(l_{unin})}\right)\delta_x(t) = 0. \tag{28}$$

According to Eq. 28, the performance of force control greatly depends on the file insertion depth unless the file flexibility compensator is implemented and the gain k_f is selected such that

$$k_f b_a \gg \frac{k_a}{k_{defl}(l_{unin})}. \tag{29}$$

Moreover, the impact of an overestimated l_{unin}—which leads to an overestimated δ_x—is negligible in the dynamic response when $b_a \gg m_a k_f$.

To illustrate the effect of varying k_f, a numerical simulation (Fig. 11) is conducted using the parameters of an S1 file, with $m_a = 0.4$, $b_a = 40$, and $k_a = 0.8$. Insertion lengths ranging from 2 to 14 mm are tested, with the initial file deflection $\delta_x(0)$ set to 3 mm. When $k_f = 0.02$, the admittance controller exhibits inconsistent performance: files with shallow insertion respond slowly and are overdamped, while those with deeper insertion respond quickly and oscillate. In contrast, Fig. 11b shows that increasing k_f to 2 yields consistent, well-damped responses across all insertion lengths. In this case, the file flexibility compensator effectively cancels out the impact of file bending, and the dynamic response is dominated by the original admittance control gains. This validates the effectiveness of the proposed file flexibility compensator in mitigating the influence of file bending on force control.

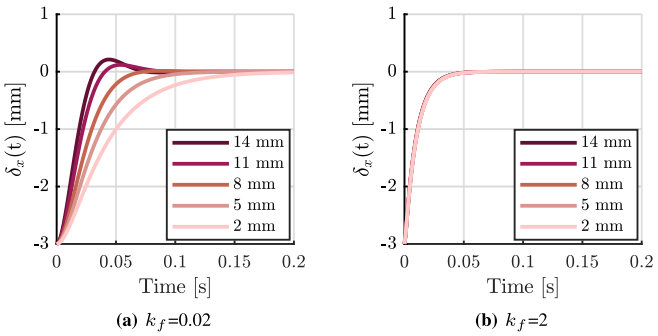

(a) k_f=0.02 (b) k_f=2

Fig. 11. Comparison of force control dynamics with varying file flexibility compensator gain k_f. When k_f is small, admittance controller performance is inconsistent as the file insertion depth changes from 14 mm to 2 mm. Increasing k_f to 2 results in consistent dynamical responses.

D. Automation of Surgical Workflow

The typical workflow for autonomous root canal cleaning and shaping is as follows.

1) Procedural Setup: The apical endpoint of the root canal is identified using preoperative CBCT scans (or micro-CT in ex vivo experiments). The working length (the path length from the root canal entrance to the apex), particularly for curved canals, is estimated using a software-assisted method [42], which reconstructs the canal trajectory and accounts for curvature. The dentist then creates an access opening to the pulp chamber and root canal, followed by attachment of the customized PTM anchor to the patient's teeth.

2) Automated Cleaning and Shaping: First, admittance control is activated with zero desired force/torque, allowing the dentist to manually position the dental handpiece by applying a dragging force and preliminarily align the endodontic file tip with the root canal entrance. At this stage, the PTM and file flexibility compensator are inactive, with $\mathbf{p}_d$, $\mathbf{p}_s$, $\mathbf{p}_f$ in Fig. 10 all set to zero. While this manual step may introduce minor alignment errors, they will be corrected during the insertion phase by the hybrid force/position controller, which autonomously adjusts the file pose to ensure precise alignment.

Subsequently, the PTM establishes a connection between the robot and the patient by connecting the detachable buckles and registering the initial relative pose, $\mathbf{p}_d$. The inner position control loop in Fig. 10 is then activated to regulate the robot–patient relative pose at $\mathbf{p}_d$.

Next, the endodontic file is automatically inserted into the root canal using hybrid position/force control. Once in place, the cleaning and shaping process begins, with the file trajectory guided by admittance control to enable compliant and autonomous navigation along the curved canal path. To prevent fracture, the file reverses if the axial torque (along the θ-axis) exceeds a predefined threshold. Please refer to Supplemental Video 1 for more details.

3) Completion: The file insertion depth is monitored throughout the procedure. Automated cleaning and shaping

IEEE Transactions on Automation Science and Engineering (T-ASE) paper, presented at ICRA 2026, Vienna, Austria.

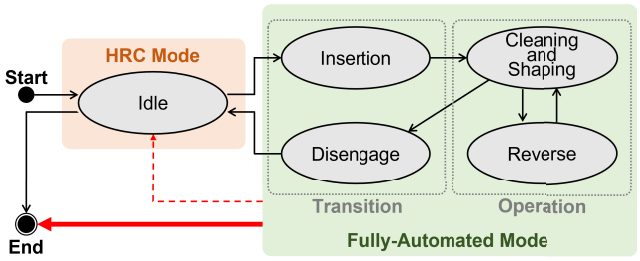

Fig. 12. Statechart diagram for autonomous root canal cleaning and shaping.

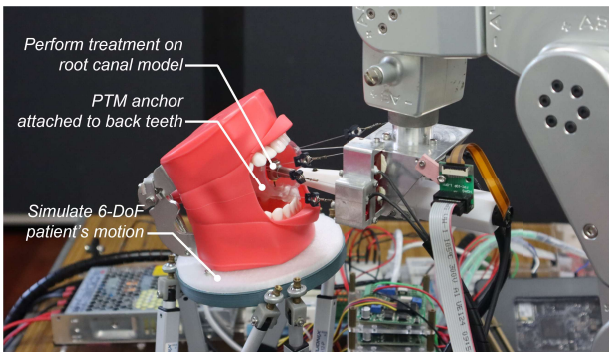

Fig. 13. Dental robot system setup with a human head phantom featuring 6-DoF simulated patient motion to mimic real surgical scenarios.

continue until the file tip reaches the working length defined by the preoperative data from the procedural setup step, marking the completion of instrumentation. Once the file reaches the working length, it is withdrawn. If the dentist decides to replace it with a larger diameter file to repeat the process, the PTM buckles must first be detached to allow file exchange, after which the robot is repositioned and the procedure resumes. After completing the treatment, the dentist detaches the PTM buckles and moves the robot aside to proceed with the remaining procedure.

The workflow for cleaning and shaping is modeled as a finite state machine to facilitate surgical automation. As illustrated in Fig. 12, there are five states: Idle, Insertion, Cleaning and Shaping, Reverse, and Disengage. The specific actions and transitions associated with each state are described below. Note that this workflow and its operational metrics were developed in consultation with dentists and are based on handpiece manuals, clinical guidelines, and experimental fine-tuning.

Idle: In the Idle state, admittance control is active for human-robot collaboration (HRC mode), while the position controller and file flexibility compensator are deactivated. Once the dentist positions the handpiece and connects the PTM, the system transitions to the Insertion state. The initial pose $\mathbf{p}_d$ is recorded when leaving the Idle state.

Insertion: In this state, the system switches to fully automated mode and activates hybrid position/force control with a desired z-axis force of 0.4 N in $\boldsymbol{\xi}_{\mathrm{d}}$. It gradually inserts the file into the target root canal until the desired contact force is detected or the insertion depth matches the previous treatment. The system then transitions to the Cleaning and Shaping state.

Cleaning and Shaping: In this state, the system autonomously performs root canal cleaning and shaping with hybrid position/force control and the endodontic file rotating at 150 rpm. The desired z-axis force gradually increases from 0.4 to 0.6, 0.8, and 1.0 N if the axial torque remains above −8 mN·m for at least 15 seconds. If the torque exceeds this threshold, the system transitions to the Reverse state. The dentist monitors whether the file tip has reached the working length or if flushing is needed. Once these conditions are met, the system moves to the Disengage state.

Reverse: This state protects against excessive axial torque by reversing the file's rotation to 250 rpm. This helps release torque and reduce the risk of file fracture. Moreover, by reversing the file, the file is slightly withdrawn. Any remaining debris inside the root canal can then be removed, ensuring a clean root cavity. The system automatically transitions back to the Cleaning and Shaping state after one second.

Disengage: In this state, the system reverses the file's rotation and withdraws it using a desired z-axis force of −0.8 N in the admittance controller. Once the file is fully extracted and the insertion depth is zero, the system transitions from the Disengage state to Idle mode, and the system resumes HRC mode. The dentist then decides whether to conclude the treatment or use another file.

In the event of unexpected issues, such as excessive axial torque despite file rotation reversal, loose PTM strings, reaching the string potentiometer's stroke limit, the system will switch to HRC mode and await troubleshooting. Loose strings are detected by a significantly large condition number of the Jacobian matrix $\mathbf{J}_{\mathbf{l}}$ (Eq. 6). If a hazardous situation is detected, such as sudden patient movement or external interference with the PTM strings (both resulting in excessively large interaction forces), the system will halt motion and terminate the automated procedure. In both emergency scenarios, file rotation will also cease immediately.

V. Experimental Validations

The proposed dental robot system for autonomous root canal cleaning and shaping was prototyped and validated through experiments. In addition to evaluating key components—such as PTM accuracy, file deflection compensation, and robot-patient alignment—a preclinical test was conducted to assess the overall system performance.

A. System Prototype

The prototyped dental robot system (see Fig. 13) was controlled via EtherCAT using an NI LabVIEW Real-Time Target (Intel Core i7-3770). This real-time controller also acquired measurements from the force/torque sensor and PTM. A separate personal computer (Intel Core i7-8700) hosted the graphical user interface (GUI), as illustrated in Fig. 14, which visualizes the root canal 3D model and the robotic system. The virtual manipulator executes synchronous 6-DoF motions by receiving 6-axis joint data via UDP. During autonomous cleaning and shaping, the GUI provides real-time visual feedback on the operation state and file insertion depth, enabling close monitoring and intervention if necessary.

IEEE Transactions on Automation Science and Engineering (T-ASE) paper, presented at ICRA 2026, Vienna, Austria.

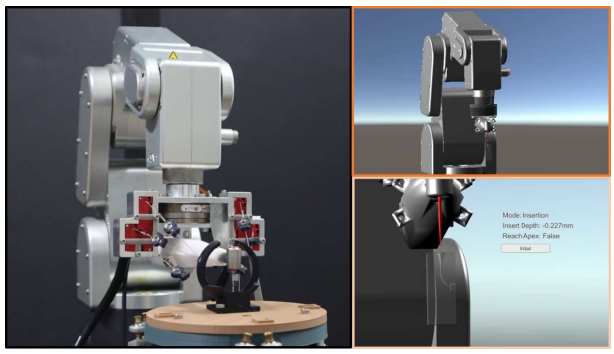

(a) Graphical user interface

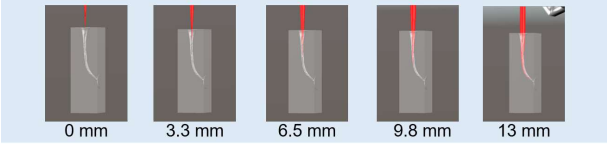

(b) Insertion depth monitor

Fig. 14. Graphical user interface (GUI) of the dental robot system. The GUI demonstrates the real-time interaction between the robot and the root canal. The pre-scanned CT model of the root canal allows dentists to supervise the surgical progress inside the canal. This feature is unachievable in conventional manual surgery. (a) The GUI. (b) Surgical progress demonstrated by file insertion depth. The endodontic file is marked in red.

TABLE II
CONTROL PARAMETERS OF THE DENTAL ROBOT

Axis	k_p	k_d	m_a	b_a	k_a	k_f
x	5.0	0.0015	0.4	40	0.8	2
y	5.0	0.0015	0.4	40	0.8	2
z	5.0	0.0015	0.4	40	1.6	0
ϕ	1.5	0.0005	0.001157	0.1157	1.6	0
ψ	1.5	0.0005	0.001633	0.1633	1.6	0
θ	1.5	0.0005	0.001208	0.1208	0	0

Fig. 14b illustrates the surgical progress, which dynamically updates the file insertion depth throughout the procedure.

The control parameters of the robotic system were determined experimentally and are presented in Tab. II. Specifically, the admittance controller parameters (m_a, b_a) were designed based on the estimated mass of the handpiece and a target settling time of 0.05 s. The scaling gains (k_a, k_f) were selected to optimize robot-patient alignment performance.

B. Evaluation of Relative Pose Estimation

This subsection evaluates the PTM's accuracy in pose estimation, focusing on measuring both translational and rotational motions. The PTM base was securely fixed to the table, while its teeth anchor (circular bite block structure) was attached to the end effector of the 6-DoF robotic manipulator (Fig. 15). The manipulator, with a path accuracy of 0.1 mm [31], simulated patient motion and moved the PTM's teeth anchor. The resulting kinematic chain is expressed as:

$$ {}^{G}_{R}\mathbf{T} = {}^{G}_{B}\mathbf{T}\,{}^{B}_{A}\mathbf{T}\,{}^{A}_{R}\mathbf{T}. \tag{30} $$

This equation indicates that the PTM's measurements, ${}^{B}_{A}\mathbf{T}$, can be mapped to the robot arm's motion, ${}^{G}_{R}\mathbf{T}$, by applying two

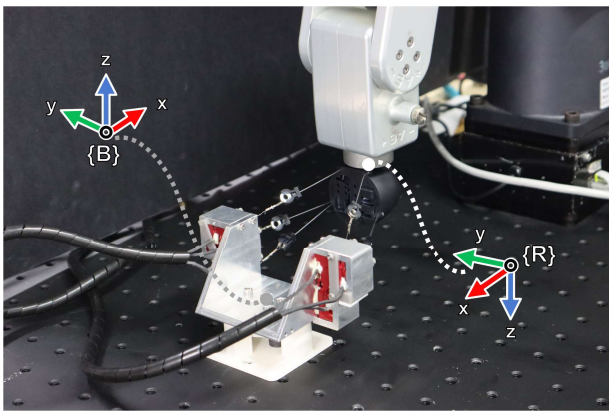

Fig. 15. Experimental setup for evaluating pose estimation. The base of the PTM was fixed on the table. The robot simulated the patient's motion and moved the anchor of the PTM. The measurements obtained from the PTM and the joint encoders of the robotic manipulator were compared.

TABLE III
ACCURACY EVALUATION OF THE PTM

Translational motion		Rotational motion	
Motion axis	Average error [mm]	Motion axis	Average error [deg]
x	0.13	ϕ	0.29
y	0.33	ψ	0.30
z	0.26	θ	0.47
x+y+z	0.53	ϕ+ψ+θ	0.73

pre-calibrated transformations, ${}^{A}_{R}\mathbf{T}$ and ${}^{G}_{B}\mathbf{T}$. In this evaluation, we compared two versions of ${}^{G}_{R}\mathbf{T}$: one derived from the PTM with the transformations applied, and the other directly from the robot's joint encoder readings.

First, the translational measuring error of the PTM was evaluated by moving the robotic manipulator 15 mm along each of the three linear axes. At each position, the Euclidean distance between the PTM measurement and the robot's joint encoder reading was calculated as measuring errors. Tab. III summarizes the average of absolute errors for each axis, all below 0.4 mm, indicating good accuracy. The y-axis error was slightly larger as it included the squareness error between the other two axes. However, the translational errors were still close to the string potentiometer's resolution of 0.2 mm. Further improvements would require using a higher-precision string potentiometer.

Subsequently, the overall translational measuring error was evaluated. The robotic manipulator was directed to traverse a three-dimensional trajectory spanning the required cylindrical workspace. During this test trajectory, all linear axes were actuated and measured simultaneously. The PTM demonstrated an average measuring error (average of Euclidean distances) of 0.5 mm, with a maximum error of 1.0 mm observed when the robotic manipulator approached the boundaries of the cylindrical workspace.

Next, the PTM's accuracy in measuring rotational motions was evaluated by commanding the robotic manipulator to track a sinusoidal trajectory along each axis, with a 5° amplitude and a 25-second period. Errors were calculated as quaternion distances between the PTM measurements and the robot's joint

IEEE Transactions on Automation Science and Engineering (T-ASE) paper, presented at ICRA 2026, Vienna, Austria.

encoders. Tab. III shows that the averages of absolute errors for each axis were all below 0.5°. An additional experiment with simultaneous rotation of all three axes demonstrated an average error of less than 0.8°. These results confirm the PTM's effectiveness as a reliable tool for real-time pose measurement and robot-patient alignment.

The developed string-based PTM presents a compelling alternative to optical tracking systems like the widely used X-Guide (X-Nav Technologies, Lansdale, PA), especially for robotic dental surgery. While the X-Guide reports a 3D implant placement accuracy of 0.38 mm [43], the PTM achieves a technical tracking accuracy of 0.53 mm.[1] A significant advantage is the PTM base unit's compact footprint of approximately $10 \times 5 \times 5$ cm^3, considerably smaller than the cart-mounted stereo camera of the X-Guide. This makes the PTM better suited for clinics with limited space. Furthermore, the PTM's string-based measurement inherently avoids the occlusion issues prevalent in optical-based tracking. This is especially critical in robotic applications, as the bulky robotic manipulator, compared to human arms, is more prone to obstructing optical markers from the camera's perspective. Although the PTM introduces the potential for mechanical wear, its robust anti-interference capabilities and seamless robotic integration position it as a highly adaptable solution for advanced robot-assisted dental procedures.

C. Evaluation of File Deflection Compensation

This subsection evaluates the effectiveness of the file flexibility compensator in estimating file deflection and improving force control performance. The parameters of the tapered beam file model were first identified and evaluated. According to Eq. 18, the endodontic file is characterized by three constants: λ, ϕ, and l_{vta}, which vary between different files. An experiment was conducted to measure file deflection for files ranging from S1 to F3 in order to determine these parameters. In this experiment, a constant lateral load of 1 N was applied to each file using the robotic manipulator's force control, with the uninserted length l_{unin} varying from 0 to 14 mm (l_{ata} = 15 mm). The file deflection δ was measured as the robot's displacement while the inserted portion of the file was fixed on the table. A nonlinear least squares method was then used to fit the data and determine the constants λ, ϕ, and l_{vta}. The results of file model identification, shown in Fig. 16, indicate that the fitting curve closely matches the recorded data, with the squared norm of the residuals being less than 0.02 mm^2.

After obtaining the file flexibility model, the estimation accuracy of file deflection was evaluated. The S1 file, which shows the largest deflection in Fig. 16, was inserted into four different 3D-printed root canal models designed to cause the file to become stuck at insertion depths ranging from 2 mm to 5 mm. The robotic manipulator then applied constant lateral loads between 0.3 N and 1.0 N to the file and recorded both actual and estimated file deflections. The results, summarized in Tab. IV, show that the estimation errors were all below 0.13 mm (the maximum error was observed at l_{in} = 2 mm with a 1 N force). This demonstrates that the identified file flexibility model accurately estimated the file deflection caused by lateral contact forces between the endodontic file and root canals.

[1]The X-Guide value represents a clinical outcome measure that includes factors such as surgical execution, task complexity, and operator skill. The system's intrinsic tracking accuracy has not been reported in the literature, so these values should be interpreted in this context.

TABLE IV
EVALUATION OF FILE DEFLECTION ESTIMATION

Canal A (Insertion depth = 2 mm)				
Force [N]	0.3	0.5	0.7	1.0
Est [mm]	0.43±0.02	0.88±0.03	1.24±0.02	1.91±0.02
GT [mm]	0.43±0.00	0.89±0.01	1.29±0.00	2.03±0.01
Err [mm]	0.01±0.01	-0.01±0.03	-0.04±0.02	-0.10±0.02
Canal B (Insertion depth = 3 mm)				
Force [N]	0.3	0.5	0.7	1.0
Est [mm]	0.51±0.02	0.76±0.03	1.03±0.02	1.45±0.02
GT [mm]	0.47±0.01	0.73±0.00	1.05±0.00	1.45±0.00
Err [mm]	0.04±0.02	0.03±0.03	-0.02±0.02	0.00±0.02
Canal C (Insertion depth = 4 mm)				
Force [N]	0.3	0.5	0.7	1.0
Est [mm]	0.23±0.01	0.47±0.01	0.78±0.02	1.17±0.01
GT [mm]	0.32±0.00	0.57±0.01	0.81±0.01	1.14±0.01
Err [mm]	-0.09±0.01	-0.09±0.01	-0.03±0.03	0.03±0.01
Canal D (Insertion depth = 5 mm)				
Force [N]	0.3	0.5	0.7	1.0
Est [mm]	0.15±0.00	0.32±0.01	0.51±0.01	0.74±0.02
GT [mm]	0.23±0.00	0.30±0.00	0.57±0.01	0.81±0.01
Err [mm]	-0.08±0.00	0.02±0.01	-0.06±0.01	-0.06±0.02

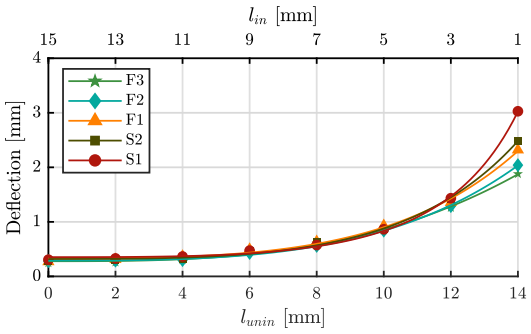

Fig. 16. Identification of file flexibility model. The deflection of each file under 1 N static lateral load, applied with varying l_{unin}, was recorded. The nonlinear least squares method was then applied to fit the model parameters. The results show that the fitting curves well align the data points with the squared 2-norm of the residual under 0.02 mm^2.

Finally, the performance of the force control incorporating the file flexibility compensator was evaluated. In this experiment, a linear platform made contact with the endodontic file at various insertion depths l_{in} while in motion. Five trials were conducted for each case. The movement profile and experimental results are presented in Fig. 17. In the absence of file flexibility compensation, i.e., only admittance control was applied, severe oscillations were observed when the insertion depth was large, leading to significant errors in the steady state (see Fig. 17a, after t = 1.25 s). In particular, when l_{in} = 14 mm, the robot motion was overly driven by the admittance controller. This indicates that admittance control is not appropriate for all file insertion depths unless file deflection is accounted for. Conversely, Fig. 17b demonstrates improved performance after compensating for file deflection. Despite potential delays in the force sensor's dynamics, the tracking

IEEE Transactions on Automation Science and Engineering (T-ASE) paper, presented at ICRA 2026, Vienna, Austria.

TABLE V

TRACKING ERROR AND CONTACT FORCE/TORQUE DURING ROBOT-PATIENT ALIGNMENT EXPERIMENT

Speed [mm/s]	e_x	e_y [mm]	e_z	e_ϕ	e_ψ [deg]	e_θ	f_x	f_y [N]	f_z	τ_x	τ_y [mN · m]	τ_z
(a) Admittance Control Only												
2.5	2.3±0.1	3.1±0.2	0.8±0.1	4.7±0.3	3.5±0.1	3.9±0.2	0.45±0.01	0.33±0.02	0.22±0.00	3.4±0.2	2.9±0.1	1.9±0.0
2.0	2.5±0.3	2.8±0.5	0.7±0.2	4.4±0.6	4.0±0.4	3.9±0.3	0.34±0.00	0.23±0.00	0.23±0.00	2.7±0.0	2.0±0.2	2.2±0.2
1.5	2.3±0.1	2.5±0.1	0.6±0.1	3.8±0.1	4.5±0.6	3.9±0.2	0.28±0.00	0.19±0.00	0.22±0.00	2.3±0.0	2.4±0.1	**1.1**±0.0
(b) Admittance Control with File Flexibility Compensator												
Speed [mm/s]	e_x	e_y [mm]	e_z	e_ϕ	e_ψ [deg]	e_θ	f_x	f_y [N]	f_z	τ_x	τ_y [mN · m]	τ_z
2.5	2.6±0.2	2.5±0.3	0.6±0.1	3.8±0.4	2.9±0.0	4.1±0.2	0.36±0.01	0.23±0.00	0.22±0.00	**1.8**±0.0	**1.5**±0.0	2.7±0.2
2.0	2.7±0.3	2.8±0.5	0.6±0.1	4.4±0.7	3.1±0.3	4.2±0.2	0.28±0.00	0.18±0.00	0.22±0.00	2.3±0.0	**1.5**±0.0	1.6±0.0
1.5	2.5±0.2	2.9±0.6	0.6±0.2	4.2±0.5	3.4±0.3	4.3±0.2	**0.23**±0.00	0.15±0.00	0.22±0.00	**2.1**±0.0	2.0±0.0	1.3±0.0
(c) Hybrid Position/Force Control												
Speed [mm/s]	e_x	e_y [mm]	e_z	e_ϕ	e_ψ [deg]	e_θ	f_x	f_y [N]	f_z	τ_x	τ_y [mN · m]	τ_z
2.5	**0.6**±0.1	**0.8**±0.1	**0.5**±0.1	**1.0**±0.0	**1.2**±0.1	**1.0**±0.0	**0.27**±0.02	**0.13**±0.01	**0.21**±0.01	2.4±0.3	2.5±0.4	**1.4**±0.2
2.0	**0.6**±0.1	**0.5**±0.0	**0.4**±0.1	**0.7**±0.0	**1.2**±0.1	**0.8**±0.0	**0.23**±0.03	**0.13**±0.01	**0.21**±0.01	**2.2**±0.1	3.1±0.0	**1.0**±0.0
1.5	**0.5**±0.1	**0.6**±0.1	**0.3**±0.0	**0.8**±0.1	**0.7**±0.1	**0.8**±0.2	**0.23**±0.03	**0.13**±0.04	**0.21**±0.00	3.0±0.4	**1.8**±0.3	3.3±0.2

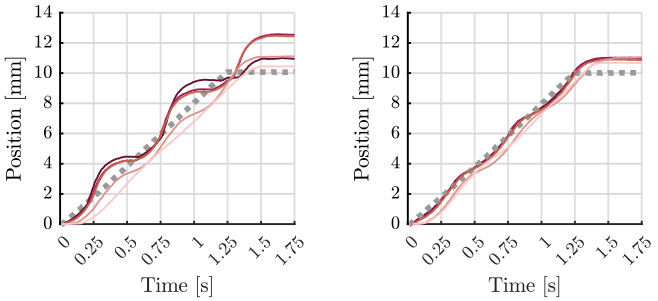

(a) Without compensation **(b)** With compensation

Fig. 17. Evaluation of the file flexibility compensator with various file insertion depth l_{in}. In this experiment, the linear platform made contact with the endodontic file at different l_{in} and moved along the ramp reference trajectory (▪▪▪▪). We recorded and compared the motion trajectories of the dental robot in response to the lateral contact force. File insertion depths (l_{in}): 14 mm (——), 11 mm (——), 8 mm (——), 5 mm (——), and 2 mm (——). (a) Before applying the compensator, the robot motion varied with different file insertion depths. In particular, when the insertion depth was set as 14 mm (——), the robot motion was overly driven by the admittance controller, causing a significant oscillation. (b) Upon applying the compensator, the robot's motion trajectories exhibited increased consistency with changes in file insertion depth. Additionally, the magnitudes of oscillation were reduced.

errors were significantly smaller than in the previous case. The robot's motion trajectories exhibited increased consistency with changes in the file insertion depth l_{in}, and the magnitudes of oscillation were also reduced.

D. Evaluation of Robot-Patient Alignment

This experiment evaluates the performance of real-time robot-patient alignment under various control strategies. We used a 6-DoF Stewart platform with a root canal model as the patient motion simulator (Fig. 13), which is independently controlled by an NI myRIO-1990 controller. The dental robot operated autonomously without communicating with the patient motion simulator, achieving real-time alignment under 6-DoF patient motions. The motions of both the robot and the patient motion simulator were recorded using a motion capture system (Impulse X2E, PhaseSpace Inc., San Leandro, CA). For coordinate system establishment, seven active markers were mounted on the robotic manipulator and the patient motion simulator, with each device having three markers. An additional marker was placed on the base of the endodontic file to obtain more accurate file position data. The position data were then transformed into the patient's frame $\{P\}$ to calculate alignment error based on Euclidean distances.

This experiment analyzed and compared the performance of different control schemes for robot-patient alignment: (a) Admittance control only, as previously implemented and reported in [18]; (b) Admittance control with the file flexibility compensator, without involving the PTM; and (c) the proposed 6-DoF hybrid position/force control. In this experiment, the endodontic file was statically inserted into the acrylic root canal model by applying a desired z-axis force of 0.2 N in the file frame {F} through the admittance controllers. The patient motion simulator moved along a slanted circular trajectory within the required cylindrical workspace, with a radius of 20 mm and a depth of 20 mm. Additionally, the roll, pitch, and yaw angles of the patient motion simulator followed a sinusoidal trajectory with an amplitude of 5 degrees. Various speeds of the 6-DoF patient's motion were tested, with average velocities of 1.5, 2.0, and 2.5 mm/s, respectively. The alignment error and contact force while using different controllers were recorded, as documented in Tab. V. Fig. 18 illustrates the trajectories of both the patient motion simulator and the dental robot, with an average speed of 2.0 mm/s.

The alignment errors under the first two control schemes, namely (a) Admittance control only and (b) Admittance control with file flexibility compensator, were analyzed. The speed of the motion did not significantly affect the tracking results. Fig. 18 indicates that both controllers exhibited a minor phase delay when tracking translational motions. Additionally, neither controller adequately addressed the rotational motions due to the conical shape of the root canal. Notably, the dental robot failed to align with the patient in the θ-axis because the admittance controller was intentionally disabled. This was done to prevent the reactive torque generated by file rotation from interfering with robot-patient alignment.

IEEE Transactions on Automation Science and Engineering (T-ASE) paper, presented at ICRA 2026, Vienna, Austria.

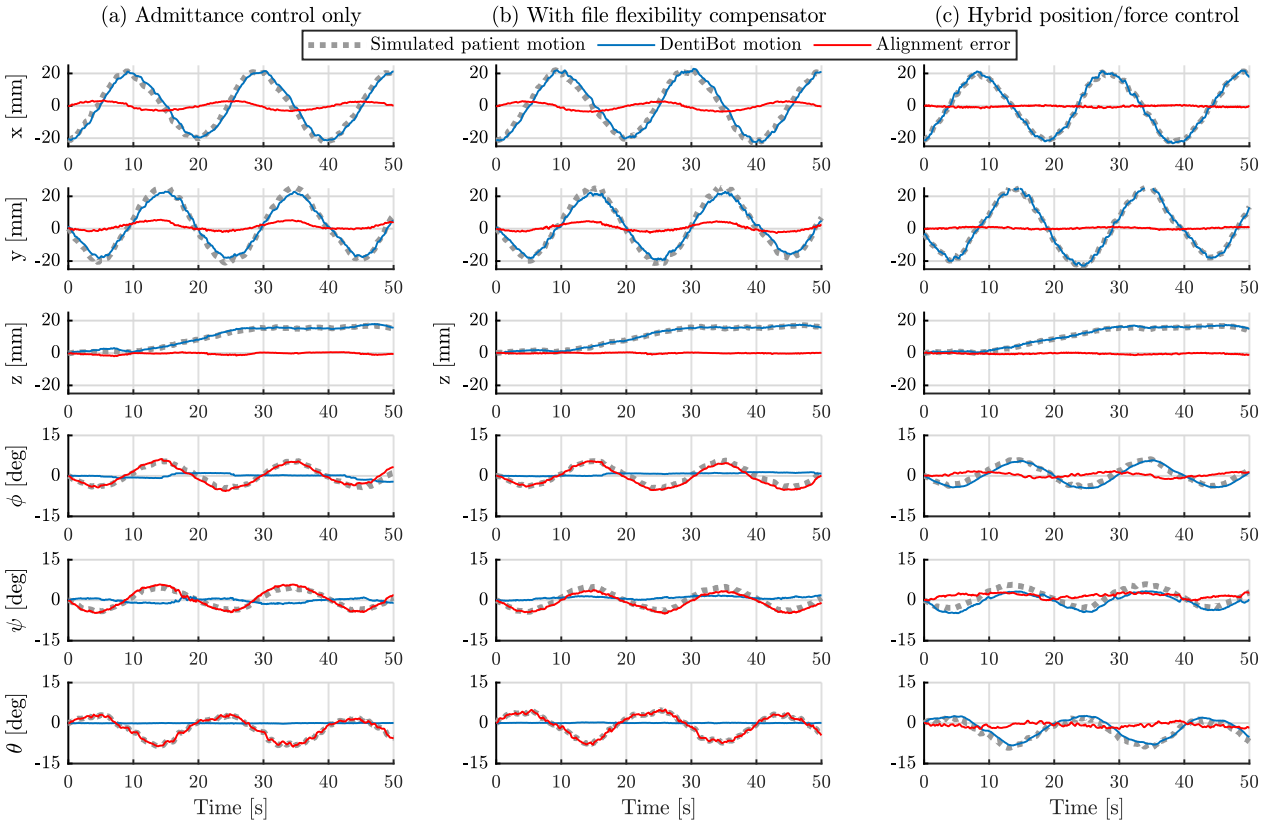

Fig. 18. Comparison of real-time robot-patient alignment under different control methods: (a) Admittance control only; (b) Admittance control with the file flexibility compensator; and (c) the proposed 6-DoF hybrid position/force control. The intraoperative patient's motions (▪▪▪▪) were simulated by the 6-DoF patient motion simulator. As indicated by the alignment errors (——), the dental robot (——) was unable to adapt to the patient's attitude changes using only the admittance controller, and there were minor delays in the translational DoFs. While the file flexibility compensator decreased the force and torque exerted on the endodontic file, it did not enhance the alignment accuracy. However, the proposed hybrid position/force controller addressed alignment errors in both translational and rotational DoFs.

Next, the alignment errors when using (b) Admittance control with file flexibility compensator and (c) 6-DoF hybrid position/force controller were compared. The integration of the PTM resulted in significant improvements in all axes. The phase delay in translational DoFs was eliminated, leading to alignment errors below 1 mm. Moreover, the dental robot accurately tracked the patient's rotational motions, achieving average errors of approximately 1.0-1.5 degrees, whereas the other two force controllers did not account for rotational tracking. The system specification (S3) regarding the error tolerance for patient motion tracking was met. These results clearly demonstrate the substantial enhancement in real-time alignment performance achieved by incorporating the PTM and employing the hybrid position/force control approach.

The average force and torque applied to the endodontic file during the alignment experiment are summarized in Tab. V. As anticipated, both force and torque increased with the velocity of the patient's movement. It is important to note that these measurements may be influenced by the sensor's measurement uncertainty; however, performance can still be reliably analyzed through comparison, given the sensor's high resolution.

When comparing different controllers, both (b) admittance control with the file flexibility compensator and (c) the 6-DoF hybrid position/force controller significantly reduced contact forces compared to (a) admittance control alone. At a speed of 1.5 mm/s, the p-value for the contact forces along the y-axis using admittance control with and without the file flexibility compensator was less than 0.0004, while the p-value between admittance control and the proposed hybrid control was 0.021, both indicating statistically significant differences. These results show that the flexibility compensator reduces undesired forces due to file misalignment and deflection, while the PTM further lowers contact forces through precise robot-patient alignment. In conclusion, the proposed controller achieved the lowest alignment errors and contact forces, ensuring the safety of dental robot during autonomous RCT.

E. Preclinical Evaluation of Autonomous Root Canal Cleaning and Shaping

This subsection evaluates the overall system performance in autonomous cleaning and shaping, utilizing root canal models and performance indices similar to those used in dental departments for training and assessing students. The surgical workflow depicted in Sec. IV-D was employed. A 1:1 human mouth model, carried by the 6-DoF patient motion simulator, was used during the preclinical evaluation, as illustrated in Fig. 13. The simulator followed random trajectories recorded from three individuals who moved their heads and jaws arbitrarily while reclining in a chair. Since the human mouth model cannot automatically clench its jaw, the recorded head and jaw motions were combined and fed into the simulator to replicate

IEEE Transactions on Automation Science and Engineering (T-ASE) paper, presented at ICRA 2026, Vienna, Austria.

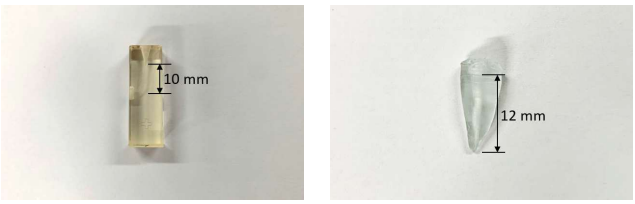

(a) Acrylic model **(b)** 3D-printed tooth

Fig. 19. In the preclinical evaluation, autonomous root canal cleaning and shaping were performed on (a) acrylic models and (b) 3D-printed resin teeth, both of which are commonly used in dental training and clinical practice. See the Supplemental Video 1 for more details.

the same movement for the model's lower jaw. The motion trajectories covered a cubic volume of $20 \times 20 \times 20$ mm^3. The average motion speed was 1.8 mm/s.

The evaluation involved testing two types of root canal models. Model A was an acrylic root canal model (Fig. 19a), commonly used for dental training. Model B consisted of 3D-printed teeth (Phrozen Sonic Mighty Revo 14K SLA printer, using ABS-like transparent resin [FeaSun FM1000], with a layer thickness of 50 μm and XY resolution of 16.8 μm), based on real human root canal anatomy (Fig. 19b). For each type, five models with subtle anatomical differences were tested. All models underwent micro-CT scanning (SkyScan 1076, Bruker Corp., Billerica, MA; resolution: 0.08 mm in all three axes) before and after the robot-assisted procedure for subsequent quantitative analysis. The morphology was segmented in 3D Slicer using thresholding and exported as STL files without smoothing or mesh simplification. The resolution and accuracy of both the 3D printer and the micro-CT system are at least one order of magnitude higher than those of the robotic system, ensuring the reliability of the results.

Prior to the autonomous procedure, the dentist selected the appropriate endodontic file type. For the acrylic models, three files (S1, S2, and F1) with increasing diameters were used. For the 3D-printed teeth, three additional files (F1, F2, and F3) were used to further enlarge the root canal cavity. Then, the dentist attached the teeth anchor to the target tooth (lower first molar), positioned the endodontic file at the root canal entrance, and connected the detachable buckles of the PTM. As shown in Fig. 13, the customized teeth anchor prevented the PTM strings from interfering with the patient's teeth and lips. The average preparation time—-measured from the placement of the teeth anchor on the phantom to the start of automatic insertion–was approximately 2 minutes for a trained user (see Supplemental Video 1). The duration of the autonomous cleaning and shaping process varied based on the size and shape of the root canal models. In general, narrower root canals required more time for the dental robot to reach the working length. However, the maximum time needed, even for a root canal that was progressively enlarged with each required file, remained under 20 minutes.

Fig. 20 illustrates the robot-patient relative motion and corresponding force/torque measurements during a preclinical trial. Along the x- and y-axes, although the PTM and inner-loop position control regulated the relative pose, small misalignments persisted, leading to increased contact forces

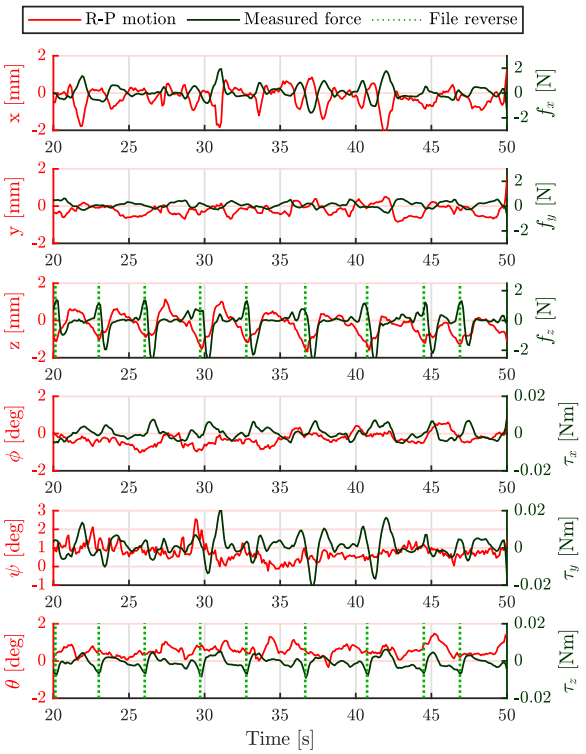

Fig. 20. Robot-Patient relative motion (R-P motion) and force/torque measurements, represented in the frame $\{F\}$, during the preclinical evaluation. Vertical green dashed lines mark instances where axial torque exceeded the threshold, triggering file reversal.

TABLE VI
PRECLINICAL EVALUATION RESULTS

Model ID	Root Canal Volume before/after [mm^3]	Enlarge Ratio	Root Canal Length before/after [mm]	Sucess? [Y/N]
A1	1.14 / 2.71	2.38	10.29 / 9.94	Y
A2	0.95 / 3.65	3.84	10.01 / 10.13	Y
A3	0.98 / 3.52	3.59	10.32 / 10.18	Y
A4	0.90 / 2.47	2.74	10.34 / 10.21	Y
A5	0.90 / 2.47	2.74	9.88 / 9.97	Y
B1	3.04 / 3.47	1.14	8.45 / 8.41	Y
B2	3.94 / 4.58	1.16	9.96 / 10.00	Y
B3	2.09 / 2.52	1.21	7.75 / 7.56	Y
B4	4.36 / 7.36	1.69	14.34 / 13.91	Y
B5	4.96 / 7.58	1.53	13.94 / 13.87	Y

between the endodontic file and canal wall. The force controller compensated by adjusting the robot pose to maintain file alignment and reduce contact forces. As a result, the motion and force trajectories exhibited negatively correlated patterns (e.g., positive motion with negative force, and vice versa). Along the z-axis, the file gradually advanced into the root canal until the torque around the θ-axis exceeded a predefined threshold (-8 mN·m). At that point (indicated by vertical green dashed lines), the robot initiated a reversal motion, retracting the file to release the accumulated axial force and torque.

The results of the preclinical evaluation are summarized in Tab. VI. A trial is deemed successful if the file reaches the

IEEE Transactions on Automation Science and Engineering (T-ASE) paper, presented at ICRA 2026, Vienna, Austria.

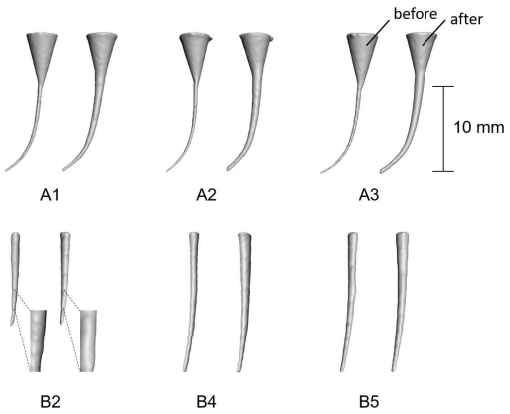

Fig. 21. CT scans of the representative root canal models tested in the preclinical evaluation. Model A denotes acrylic models and Model B denotes 3D-printed resin teeth. The root canals were enlarged and well-shaped after autonomous cleaning and shaping. In particular, the wall of the root canal (see Model B2) appeared smoother post-treatment.

working length without ledging or fracture. All procedures were completed successfully, even under arbitrary patient motions, with no instances of file fracture or ledging. The acrylic models showed a larger enlargement ratio, which is attributed to their narrower root canal pathways. Overall, there was no significant difference in root canal length after treatment, demonstrating the effectiveness of intraoperative monitoring of file insertion depth. In some models, a slight reduction in root canal length was noted following the autonomous procedure, likely due to debris accumulation near the apex.

Fig. 21 shows the CT scan results of the representative root canal models tested in the preclinical evaluation. Compared to the 3D-printed resin models, the acrylic models exhibited a greater degree of curvature. Despite this, the dental robot successfully completed the cleaning and shaping process autonomously. As shown in Fig. 21, the root canals were effectively enlarged and well-shaped. Notably, Model B2 displayed a smoother root canal wall following the robot-assisted procedure. These results demonstrate the robot's capability to autonomously perform the cleaning and shaping step in RCT.

VI. Conclusion

This paper presents the system and control methods for autonomous RCT. The clinical requirements for an adequate workspace, real-time force guidance, and accurate patient motion tracking are effectively addressed through the integration of a 6-DoF robotic manipulator, a 6-axis force/torque sensor, and a novel string-based Patient Tracking Module, respectively. A file flexibility compensator is developed to mitigate file bending caused by misalignment between the endodontic file and the root canal. Furthermore, the implementation of a hybrid position/force control scheme enables autonomous file manipulation while maintaining the relative pose between the robotic system and the patient.

Extensive experimentation has demonstrated that each system component meets clinical requirements. Notably, the dental robot "DentiBot" achieves precise alignment with the patient, which is not possible using force control alone. Preclinical evaluations on acrylic models and 3D-printed teeth provide strong evidence that the system can autonomously and effectively clean and shape root canals, even under arbitrary patient motions.

Future work will focus on integrating automated file selection and an apex locator. Efforts will also be directed toward automating other critical RCT steps, such as access opening and obturation. These advancements will further enhance the robotic system and set new standards for autonomous endodontic treatment, contributing to improved clinical outcomes and patient care.

Acknowledgment

The authors would like to express their gratitude to Yi-Chan Li, Zi-Hao Huang, Shao-Lun Chang, Mu-Ting Mao, Kun-Chan Wu, Chia-Ying Lin, and Dr. Chen-Yu Chan for their invaluable technical support in this project.

References

[1] L. S. Mattos, D. G. Caldwell, G. Peretti, F. Mora, L. Guastini, and R. Cingolani, "Microsurgery robots: Addressing the needs of high-precision surgical interventions," *Swiss Med. Weekly*, vol. 146, no. 4344, Oct. 2016, Art. no. w14375.

[2] L. Liu, M. Watanabe, and T. Ichikawa, "Robotics in dentistry: A narrative review," *Dentistry J.*, vol. 11, no. 3, p. 62, Feb. 2023.

[3] S. L. Bolding and U. N. Reebye, "Accuracy of haptic robotic guidance of dental implant surgery for completely edentulous arches," *J. Prosthetic Dentistry*, vol. 128, no. 4, pp. 639–647, Oct. 2022.

[4] X. Sun, Y. Yoon, J. Li, and F. D. McKenzie, "Automated image-guided surgery for common and complex dental implants," *J. Med. Eng. Technol.*, vol. 38, no. 5, pp. 251–259, Jul. 2014.

[5] J. Li et al., "A compact dental robotic system using soft bracing technique," *IEEE Robot. Autom. Lett.*, vol. 4, no. 2, pp. 1271–1278, Apr. 2019.

[6] Y. Feng et al., "An image-guided hybrid robot system for dental implant surgery," *Int. J. Comput. Assist. Radiol. Surgery*, vol. 17, no. 1, pp. 15–26, Jan. 2022.

[7] H. Wang, "Automation in dental and eye surgery," Ph.D. dissertation, Dept. Mech. Aerosp. Eng., University of California, Los Angeles, CA, USA, 2022.

[8] J. L. Gutmann and P. E. Lovdahl, *Problem Solving in Endodontics: Prevention, Identification and Management*. Hoboken, NJ, USA: Wiley, 2010.

[9] Y.-H. Liang and L. Yue, "Evolution and development: Engine-driven endodontic rotary nickel-titanium instruments," *Int. J. Oral Sci.*, vol. 14, no. 1, p. 12, 2022.

[10] B. Sattapan, G. J. Nervo, J. E. Palamara, and H. H. Messer, "Defects in rotary nickel-titanium files after clinical use," *J. Endodontics*, vol. 26, no. 3, pp. 161–165, Mar. 2000.

[11] A. Y. Alqutaibi, H. H. Hamadallah, A. M. Aloufi, H. A. Qurban, M. M. Hakeem, and M. A. Alghauli, "Contemporary applications and future perspectives of robots in endodontics: A scoping review," *Int. J. Med. Robot. Comput. Assist. Surgery*, vol. 20, no. 5, p. 70001, 2024.

[12] J. Dong, S. Y. Hong, and G. Hesselgren, "WIP: A study on the development of endodontic micro robot," in *Proc. IJME-INTERTECH Conf.*, 2007, pp. 104–110.

[13] J. Dong and S. Y. Hong, "Design of Z axis actuator and quick tool change assembly for an endodontic micro robot," in *Proc. ASME Int. Mech. Eng. Congr. Expo.*, Jan. 2010, pp. 507–511.

[14] M. Li, Y.-H. Liu, and Q. Huang, "An optimized haptic interaction model based on support vector regression for evaluation of endodontic shaping skill," in *Proc. IEEE Int. Conf. Robot. Biomimetics (ROBIO)*, Dec. 2007, pp. 617–622.

[15] D. Wu, J. Jiang, J. Pan, K. Qian, and Z. Xue, "Root canal preparation robot based on guiding strategy for safe remote therapy: System design and feasibility study (2023)," *IEEE/ASME Trans. Mechatronics*, vol. 30, no. 1, pp. 84–95, Jan. 2025.

[16] T. Gulrez, A. K. Shahid, U. Sana, and N. G. Chaudhary, "Visual guided robotic endodontic therapeutic system," in *Proc. Int. Conf. Inf. Emerg. Technol.*, Jun. 2010, pp. 1–6.

IEEE Transactions on Automation Science and Engineering (T-ASE) paper, presented at ICRA 2026, Vienna, Austria.

[17] D. Dasgupta, S. Peddi, D. K. Saini, and A. Ghosh, "Mobile nanobots for prevention of root canal treatment failure," *Adv. Healthcare Mater.*, vol. 11, no. 14, Jul. 2022, Art. no. 2200232.

[18] H.-F. Cheng, Y.-C. Li, Y.-C. Ho, and C.-W. Chen, "Force-guided alignment and file feedrate control for robot-assisted endodontic treatment," in *Proc. IEEE/RSJ Int. Conf. Intell. Robots Syst. (IROS)*, Oct. 2022, pp. 1841–1847.

[19] K. C. Lim and J. Webber, "The validity of simulated root canals for the investigation of the prepared root canal shape," *Int. endodontic J.*, vol. 18, no. 4, pp. 240–246, 1985.

[20] A. Toosi, M. Arbabtafti, and B. Richardson, "Virtual reality haptic simulation of root canal therapy," *Appl. Mech. Mater.*, vol. 666, pp. 388–392, Feb. 2014.

[21] M. Sin, J. H. Cho, H. Lee, K. Kim, H. S. Woo, and J.-M. Park, "Development of a real-time 6-DOF motion-tracking system for robotic computer-assisted implant surgery," *Sensors*, vol. 23, no. 5, p. 2450, Feb. 2023.

[22] B. Yan et al., "Optics-guided robotic system for dental implant surgery," *Chin. J. Mech. Eng.*, vol. 35, no. 1, p. 55, Dec. 2022.

[23] V. Paredes-Gallardo, J. Gandia, and R. M. C. O. D. Anda, "Determination of Bolton tooth-size ratios by digitization, and comparison with the traditional method," *Eur. J. Orthodontics*, vol. 28, no. 2, pp. 120–125, 2005.

[24] R. Lähdesmäki and L. Alvesalo, "Root lengths in 47, XYY males' permanent teeth," *J. Dental Res.*, vol. 83, pp. 771–775, Nov. 2004.

[25] T. Muto and M. Kanazawa, "Linear and angular measurements of the mandible during maximal mouth opening," *J. Oral Maxillofacial Surg.*, vol. 54, no. 8, pp. 970–974, 1996.

[26] M. S. Zehnder, T. Connert, R. Weiger, G. Krastl, and S. Kühl, "Guided endodontics: Accuracy of a novel method for guided access cavity preparation and root canal location," *Int. Endodontic J.*, vol. 49, no. 10, pp. 966–972, Oct. 2016.

[27] J. Lee et al., "Three-dimensional analysis of root anatomy and root canal curvature in mandibular incisors using micro-computed tomography with novel software," *Appl. Sci.*, vol. 10, no. 12, p. 4385, Jun. 2020.

[28] M. Haapasalo and Y. Shen, "Evolution of nickel–titanium instruments: From past to future," *Endodontic Topics*, vol. 29, no. 1, pp. 3–17, Sep. 2013.

[29] (2004). *ProTaper Universal Guidelines*. Accessed: Jun. 5, 2025. [Online]. Available: https://e-ecodent.gr/images/ProductsInfo/MAILLEFER/sequence.pdf

[30] J. N. R. Martins et al., "Mechanical performance and metallurgical features of ProTaper universal and 6 replicalike systems," *J. Endodontics*, vol. 46, no. 12, pp. 1884–1893, Dec. 2020.

[31] T. A. Khaled, O. Akhrif, and I. A. Bonev, "Dynamic path correction of an industrial robot using a distance sensor and an ADRC controller," *IEEE/ASME Trans. Mechatronics*, vol. 26, no. 3, pp. 1646–1656, Jun. 2021.

[32] C. Yang et al., "A four-point measurement model for evaluating the pose of industrial robot and its influence factor analysis," *Ind. Robot: Int. J.*, vol. 44, no. 3, pp. 343–352, May 2017.

[33] S. G. Vougioukas, "Bias estimation and gravity compensation for force-torque sensors," in *Proc. 3rd WSEAS Symp. Math. Methods Comput. Techn. Electr. Eng.*, Dec. 2001, pp. 82–85.

[34] F. Thomas, E. Ottaviano, L. Ros, and M. Ceccarelli, "Performance analysis of a 3-2-1 pose estimation device," *IEEE Trans. Robot.*, vol. 21, no. 3, pp. 288–297, Jun. 2005.

[35] J. W. Jeong, S. H. Kim, and Y. K. Kwak, "Kinematics and workspace analysis of a parallel wire mechanism for measuring a robot pose," *Mechanism Mach. Theory*, vol. 34, no. 6, pp. 825–841, Aug. 1999.

[36] M. Raghavan, "The Stewart platform of general geometry has 40 configurations," *J. Mech. Design*, vol. 115, no. 2, pp. 277–282, Jun. 1993.

[37] C. C. Nguyen, Z.-L. Zhou, S. S. Antrazi, and C. E. Campbell, "Efficient computation of forward kinematics and Jacobian matrix of a Stewart platform-based manipulator," in *Proc. IEEE SOUTHEASTCON*, Feb. 1991, pp. 869–874.

[38] Z. Xie, G. Li, G. Liu, and J. Zhao, "Optimal design of a stewart platform using the global transmission index under determinate constraint of workspace," *Adv. Mech. Eng.*, vol. 9, no. 10, Oct. 2017, Art. no. 168781401772088.

[39] DENTSPLY International. *Protaper Universal System Brochure*. Accessed: Jun. 5, 2025. [Online]. Available: https://www.dentsplysirona.com/content/dam/master/ecom/regions-countries/north-america/product-procedure-brand/endodontics/product-categories/files-motors-lubricants/rotary-and-reciprocating-files/protaper-universal/documents/END-Brochure-ProTaper-Universal-Rotary-Files-EN.pdf

[40] R. F. Gibson, *Principles of Composite Material Mechanics*. Boca Raton, FL, USA: CRC Press, 2016.

[41] A. Winkler and J. Suchy, "Implicit force control of a position controlled robot—A comparison with explicit algorithms," *Int. J. Comput. Inf. Eng.*, vol. 9, no. 6, pp. 1447–1453, 2015.

[42] S. N. Sisli and O. Gülen, "Root canal length measurement of molar teeth using cone-beam computed tomography (CBCT): Comparison of two-dimensional versus three-dimensional methods," *Eur. Oral Res.*, vol. 55, no. 2, pp. 94–98, Feb. 2021.

[43] R. W. Emery, S. A. Merritt, K. Lank, and J. D. Gibbs, "Accuracy of dynamic navigation for dental implant placement–model-based evaluation," *J. Oral Implantol.*, vol. 42, no. 5, pp. 399–405, Oct. 2016.

Hao-Fang Cheng received the B.S. degree in mechanical engineering and the M.S. degree in electrical engineering from National Taiwan University, Taipei, Taiwan, in 2021 and 2023, respectively. His research interests include robotics, pose estimation, and control algorithms.

Yi-Ching Ho was the Director of the Postgraduate Residency Program in Endodontics. She is an Associate Professor at the Department of Dentistry, National Yang-Ming Chiao-Tung University, Taiwan. She serves as an Associate Professor at Taipei Veterans General Hospital, Taiwan. She received the Diplomate of the Board of Endodontology, Taiwan, in 2009, indicating her status as a board-certified endodontics. Additionally, she serves as a Board Examiner for the Board of Endodontology. She has contributed to numerous research articles published in peer-reviewed journals, focusing on robotic-assisted root canal treatment, optical coherence tomography in caries research, and augmented intelligence in Endodontics.

Cheng-Wei Chen (Senior Member, IEEE) received the Ph.D. degree in mechanical engineering from the University of California at Los Angeles, Los Angeles, CA, USA, in 2018. He is currently an Associate Professor of electrical engineering at the National Taiwan University, Taipei, Taiwan. His research interests include robotics, mechatronics, digital control systems, and numerical optimization.